

DC Readout in Enhanced LIGO

A Dissertation

Submitted to the Graduate Faculty of the
Louisiana State University and
Agricultural and Mechanical College
in partial fulfillment of the
requirements for the degree of
Doctor of Philosophy

in

The Department of Physics and Astronomy

DRAFT compiled September 4, 2011

by

Tobin Thomas Fricke

B.S., University of California, Berkeley, 2003

M.A., University of Rochester, 2005

August 2011

TABLE OF CONTENTS

Dedication	vi
Acknowledgments	vii
Tables	viii
Figures	ix
1. Introduction	1
1.1 Gravitational Waves	1
1.2 The Hulse-Taylor Pulsar	2
1.3 Sources of Gravitational Waves	3
1.4 Detectors	4
1.4.1 Laser interferometers	5
1.4.2 Other detectors	5
1.5 LIGO	5
1.6 Summary of changes made for Enhanced LIGO	5
1.7 The Future	6
1.8 This Dissertation	6
2 The LIGO detector	8
2.1 Arms, cavities, etc	8
2.2 A Michelson	9
2.3 Resonant cavities	11
2.3.1 Fabry-Perot field equations	11
2.3.2 the cavity pole	12
2.3.3 phase gain	12
2.3.4 power buildup	13
2.3.5 coupling	13
2.4 Michelson with Fabry-Perot arms	13
2.5 Power recycling	13
2.6 The coupled cavity pole	14
2.7 Interferometer Sensing and Control	14
2.8 Heterodyne detection	14

2.8.1	The Pound-Drever-Hall technique	15
2.9	Determination of LIGO cavity lengths and mirror reflectivities	15
2.10	Heterodyne shot noise	19
3	DC Readout	22
3.1	Principle of DC readout	22
3.2	Motivation for DC readout	22
3.2.1	Calculation of the optical gain	23
3.3	Offset	26
3.3.1	Decrease in arm power due to off-resonance operation	27
3.3.2	Decrease in power recycling gain due to power loss at the output port	27
4	Output Mode Cleaner	28
4.1	Introduction	28
4.2	General theory of mode cleaners	28
4.3	Eigenmodes	29
4.4	Physical design of the cavity	30
4.5	Requirements	30
4.6	Choosing the OMC finesse	32
4.7	Length control (LSC)	32
4.8	Input beam control (ASC)	34
4.9	Automatic gain control	36
4.10	Residual fluctuations	36
4.11	Optical characterization	36
4.11.1	Mode scan	36
4.11.2	Scattering	36
4.12	Interferometer lock acquisition	36
4.13	Beam diverter	38
4.14	The Front End	38
5	DC readout performance and noise couplings	39
5.1	Sensitivity	39
5.1.1	Measured and expected sensitivity	40
5.2	Laser and oscillator noise coupling mechanisms	41
5.2.1	Laser noises	43
5.2.2	Oscillator noises	44
5.3	Laser and oscillator noise coupling measurements	45
5.3.1	Laser noise coupling measurements	45
5.3.2	Oscillator noise coupling measurements	46
5.4	Beam jitter noise	49
5.5	Electronics noise	49
5.6	Optical spring	49
5.7	Technical radiation pressure noise	52

5.8	Nonlinearity of the DC error signal	52
5.9	Digital effects	52
5.10	Conclusion	52
6.	Blargh	53
6.1	Abbreviations	53
6.2	symbols	54
7	Appendix	55
7.1	Cavity stuff	55
7.2	The difference between PM and AM	55
7.3	The difference between PM and FM	57
7.4	Only the signal field matters	57
7.5	Optical phase conventions	58
7.6	The optical spring	58
7.6.1	Coupled oscillators	59
7.6.2	Damped oscillators	60
7.6.3	Optickle	61
7.7	Gaussian beams	61
7.8	Laser modes	62
7.9	Control theory basics	62
7.10	The Antenna Pattern	62
7.11	Shot Noise	62
7.12	Noise analysis of opamp circuits	63
7.13	References	63

Dedication

Acknowledgments

Thank you for putting up with me.

List of Tables

4.1	Output mode cleaner properties (designed and measured)	31
5.1	Interferometer properties (designed and measured)	41

List of Figures

1.1	Effect of a gravitational wave on a ring of test particles	2
1.2	EXPLORER bar detector	4
2.1	Michelson interferometer	9
2.2	Fabry-Perot Cavity	11
2.3	Illustration of cyclo-stationary shot noise	21
3.1	Frequency-domain fields in DC and RF readouts	24
3.2	Residual DARM motion	26
4.1	Beam spot at anti-symmetric port	30
4.2	Hermite-Gauss TEM modes	31
4.3	Cartoon view of dither locking	33
4.4	Modal decomposition of a displaced Gaussian	34
4.5	Drumhead dither system	35
4.6	Length Sensing and Control (LSC) control screen	37
5.1	Shot noise sensitivity limit (measured and expected)	42
5.2	Schematic diagram of the laser carrier and RF sidebands, and their associated audio-frequency sidebands.	43
5.3	Components of laser intensity noise contribution to DC readout	44
5.4	Laser intensity noise coupling (measured and modeled)	47
5.5	Laser frequency noise coupling (measured and modeled)	48
5.6	Oscillator amplitude noise coupling (measured and modeled)	50
5.7	Oscillator phase noise coupling (measured)	51
7.1	Pole-zero map of Fabry-Perot cavity reflectivity	56
7.2	Optical spring transfer function (numerical and analytic)	64
7.3	Basic active filter in the inverting amplifier configuration.	64

Abstract

Gravitational waves are ripples of space-time predicted by Einstein's theory of General Relativity. The Laser Interferometer Gravitational-wave Observatory (LIGO), part of a global network of gravitational wave detectors, seeks to detect these waves and study their sources.

The LIGO detectors were recently upgraded with the dual goals of increasing the sensitivity (and likelihood of detection) and proving techniques for Advanced LIGO, a major upgrade currently underway. As part of this upgrade, the signal extraction technique was changed from a heterodyne scheme to a form of homodyne detection called DC readout. The DC readout system includes a new optical filter cavity, the output mode cleaner, which removes unwanted optical fields at the interferometer output port.

This work describes the implementation and characterization of the new DC readout system and output mode cleaner, including the achieved sensitivity, noise couplings, and servo control systems.

1. Introduction

1.1 Gravitational Waves

Almost all of humanity's knowledge of the universe is derived from observations of electromagnetic waves. The effort to detect gravitational waves seeks to expand this knowledge by observing an entirely different field, and to further verify the correctness of the theory of general relativity.

Any theory of gravity that avoids instantaneous action at a distance must feature some kind of gravitational waves. Even Newtonian gravity can be modified to account for propagation delays from massive bodies that are the sources of attraction[1]. Gravity as we know it, however, is described by the general theory of relativity. In general relativity, spacetime is treated as a four-dimensional manifold with some intrinsic curvature. This curvature is generated by the presence of mass and energy. In the absence of forces, particles follow geodesic trajectories on this manifold. Thus, in the quintessential words of John Wheeler(?), "Space tells matter how to move, matter tells space how to curve."

This relationship between matter and curvature is made formal through the Einstein field equation, which equates (up to units) the Einstein tensor (G), encoding curvature, with the Stress-Energy tensor (T), encoding the matter and energy contents:

$$G = \frac{8\pi G}{c^4} T \tag{1.1}$$

where G is (Newton's) universal gravitational constant and c is the speed of light.

To perform calculations, we typically need to work in some coordinate basis. Thus one will work with $G_{\mu\nu}$, where μ and $\nu \in 0, 1, 2, 3$ are coordinate indices. In this notation, the Einstein tensor is given by $G_{\mu\nu} = R_{\mu\nu} - \frac{1}{2}Rg_{\mu\nu}$, where $R_{\mu\nu}$ is the Ricci curvature tensor, R is the Ricci scalar, and $g_{\mu\nu}$ is the spacetime metric. The metric plays a central role here, as it both encodes the curvature and implicitly defines the coordinate system.

To reveal the mechanism of gravitational waves, we are interested in vacuum ($T = 0$) solutions of the Einstein field equations in the weak-field limit. In the weak-field limit, we can write the metric $g_{\mu\nu}$ as the sum of the flat-space Minkowski metric $\eta_{\mu\nu}$ and a small perturbation $h_{\mu\nu}$:

$$g_{\mu\nu} = \eta_{\mu\nu} + h_{\mu\nu}$$

This is the regime of linearized gravity. Calculating out the Einstein field equation keeping only terms of first-order in h and choosing the transverse-traceless gauge, one finds (see Sean

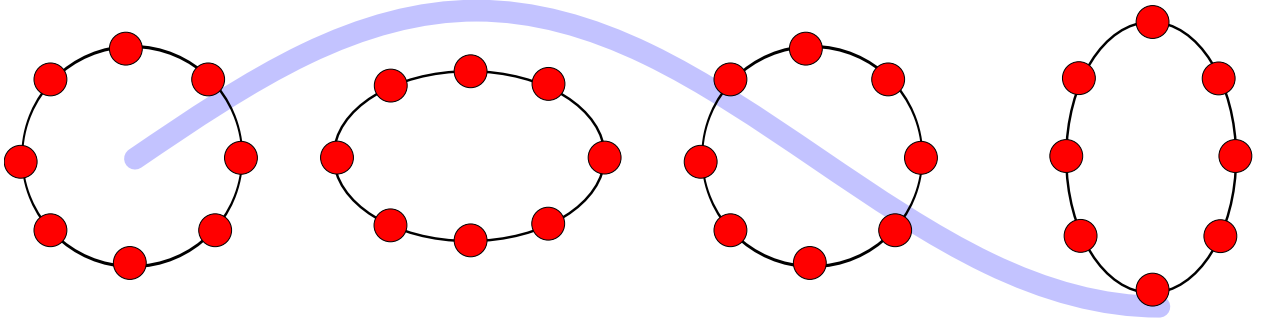


Figure 1.1: Effect of a gravitational wave (traveling into or out of the page) on a ring of non-interacting inertial test particles.

Carroll's lucid exposition in [2] for the details) a wave equation for h :

$$\left(\nabla^2 - \frac{1}{c^2} \frac{\partial^2}{\partial t^2} \right) h_{\mu\nu} = 0$$

where $h_{\mu\nu}$ has, for a wave propagating along the z axis, the form:

$$[h] = \begin{pmatrix} 0 & 0 & 0 & 0 \\ 0 & a & b & 0 \\ 0 & b & -a & 0 \\ 0 & 0 & 0 & 0 \end{pmatrix}$$

Here we see several of the essential points of gravitational waves:

- There are two independent components (polarizations)
- They travel at the speed of light
- They are manifest as a transverse tidal force on inertial objects

The amplitude of gravitational waves is quantified as the effective strain exerted on inertial test-masses.

1.2 The Hulse-Taylor Pulsar

Gravitational waves have not yet been directly detected, but very strong indirect evidence exists. Perhaps the strongest evidence is the Hulse-Taylor pulsar [3, 4]—a remarkable discovery of a binary star system in which one of the constituents is pulsar PSR B1913+16. The binary system is expected to radiate energy away into gravitational waves, causing its orbit to decay. The pulsar reveals the orbital parameters of the binary system, in particular its orbital period. Measurement of the orbital period through pulsar tracking over 30 years shows that the orbit is decaying exactly as predicted by general relativity.

Another binary system containing pulsars was discovered in 2004. In this system *both* objects are pulsars. [5, 6]

1.3 Sources of Gravitational Waves

Any system of mass accelerating in the quadrupolar or higher moments will radiate energy into gravitational waves. The effect is so weak, however, that only some of the universe's more cataclysmic events have a chance of producing waves observable on earth.

Anticipated sources of gravitational waves can be conveniently categorized as *continuous* or *transient*, and as *modeled* or *unmodeled*. There is some overlap in this division. Sources are paired with associated search efforts.

- **compact binary coalescence** — Pairs of compact objects (black holes or neutron stars) in binary orbits are expected to lose energy through gravitational waves, causing the orbit to decay until the objects finally begin to interact and merge into a single object. This inspiral process will generate a characteristic chirp signal, followed by the complex merger process and then ringdown.
- **continuous wave** — Rapidly spinning objects will generate essentially monochromatic signals, which are in turn doppler-shifted by the relative motion of the Earth and the source. This is sometimes called the pulsar search, since the primary source in this category is expected to be rapidly spinning neutron stars (such as pulsars). The search, in turn, is divided into searches for known pulsars and unknown pulsars. Pulsars which are known electromagnetically can be targetted directly, whereas unknown pulsars require a brute-force search of the parameter space.

Currently this is attacked in part through the distributed computing project Einstein@Home. One nicety of the pulsar search is that the process works equally well for analyzing radio telescope data—this has been done, resulting in the discovery of several previously unknown radio pulsars[7]. It is an open problem to find a more efficient search algorithm.

- **bursts** — Transient cataclysmic events such as supernovae will generate bursts of gravitational waves whose waveforms is not known in advance.
- **stochastic background** — In the same manner as the cosmic microwave background radiation, a cosmological background of gravitational waves is expected to exist. This is perhaps the most exotic anticipated source of gravitational waves, since its detection will inform us of the state of the universe at an age far earlier than has yet been probed. Sadly, the cosmological background is almost certainly too weak to detect in the foreseeable future.

The cacophony of unresolved astrophysical sources will also combine to produce a gravitational wave stochastic background.

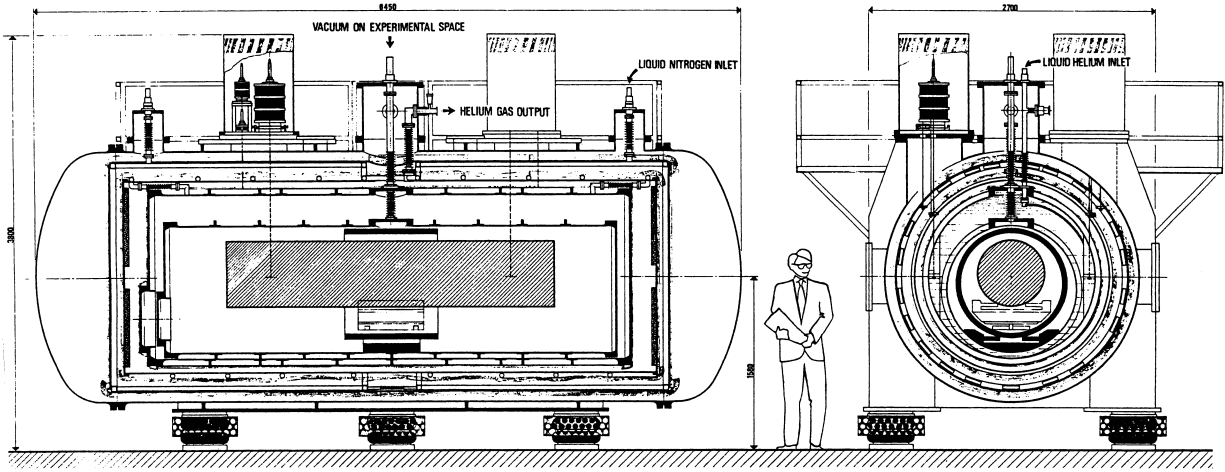


Figure 1.2: Depiction of the cryostat of the EXPLORER bar detector, which operated **somewhere** for **some time**. Illustration adapted from **a reference**.

The stochastic background search is fully coherent. In its simplest form, the search simply computes the correlation between pairs of gravitational wave detectors. This can be done in either an all-sky search or in a sky-position-dependent search. Typically, some power-law gravitational wave spectrum is assumed.

Improvements in search sensitivity can be achieved by incorporating knowledge of the expected signal waveform or spectrum; integrating over a long period of time (for continuous sources); and by looking for coincidence or coherence between multiple detectors.

The global network of gravitational wave detectors is operated as a sensor array, an interferometer composed of many interferometers.

1.4 Detectors

Gravitational waves couple to both light and matter.

The first attempts to detect gravitational waves used resonant bar detectors. In such a detector, a large cylinder of a metal alloy with a very high mechanical Q-factor is suspended in a vacuum chamber and cooled to cryogenic temperatures. A passing gravitational wave couples mechanical energy into the bar, ringing up the fundamental mechanical mode of the bar. Sensitive detectors (latter bars used SQUIDS) read out this mechanical displacement. Resonant bars are inherently narrow-band devices, sensitive to gravitational waves within a narrow linewidth about their fundamental resonance.

Bar detectors do have the advantage that they are small enough that they can be moved or re-oriented. The ALLEGRO bar detector at LSU was once rotated to modulate its overlap function with the nearby LIGO Livingston observatory.

1.4.1 Laser interferometers

Laser interferometers are now the instrument of choice in the search for gravitational waves. A gravitational wave will modulate the optical path length of light traveling transversely through it between inertial test masses. This path length modulation can be detected by a laser interferometer. The operation of laser interferometer gravitational wave detectors is the focus of this work and is detailed in the following chapters.

In terrestrial interferometers, large¹ glass cylinders serve as both super-polished mirrors and inertial test masses. These optics are hung as pendula to allow inertial freedom of the pendular resonance frequency.

References to cite in this section: [8, 9]

1.4.2 Other detectors

There are a few other mechanisms by which gravitational waves may be detected.

Pulsars serve as extremely reliable clocks, beaming a sequence of pulses towards earth whose arrival times can typically be predicted to better than a microsecond. The path of the electromagnetic waves traveling from the pulsar to earth acts in some ways like an arm of a laser interferometer: gravitational waves passing transversely to the Earth-Pulsar baseline will modulate the optical path length, producing perturbations in the arrival time of the pulsar pulses—perturbations which are correlated between observations of distinct pulsars. Pulsar timing arrays seek to analyze these correlated residuals to find evidence of gravitational waves; Hobbs [10] anticipates that pulsar timing analysis will yield detections of gravitational waves in the nanohertz regime (period 3-30 years) in the next 5-10 years.

Primordial gravitational waves will also leave their imprint on the polarization of the cosmic microwave background radiation. Many CMB polarization experiments are currently underway, searching for the faint “B-modes” in the microwave polarization.

1.5 LIGO

Construction began on the LIGO observatories in YEAR. After many years of commissioning, the detectors reached their design sensitivity in YEAR. Having met the conditions described in the science requirements document, LIGO commenced a long observational run, accumulating one year of coincident data over a period of two calendar years.

1.6 Summary of changes made for Enhanced LIGO

After the successful completion of the Initial LIGO science goals, it was decided [11, 12, 13] to attempt to further improve the detector sensitivity by aggressively implementing a few prototype Advanced LIGO technologies.

¹10 kg in Initial LIGO, 40 kg in Advanced LIGO

Changes included:

- Fancy new laser
- Renovation of the input optics to handle higher power operation, including new electro-optic modulators [14]
- Installation of an output mode cleaner, supported by a prototype of the advanced LIGO in-vacuum seismic isolation system
- New Thermal Compensation System to handle the higher power

DC readout has been implemented previously at the Caltech 40 meter prototype [15, 16] and the GEO 600 detector[17, 18, 19]. The current configuration of Virgo incorporates an output mode cleaner but uses RF heterodyne readout[20].

1.7 The Future

It is hoped that Advanced LIGO, currently under construction, will bring the first direct detection of gravitational waves and begin the era of regular detection.

Several next-generation interferometers are in the works.

The Einstein telescope [21] is a planned system of three interferometers with arms forming an equilateral triangle, to be installed in tunnels deep under Europe.

In the meantime, technological development of terrestrial laser interferometers is a vibrant field. The Advanced detectors are anticipated to be limited almost everywhere by quantum mechanical noises, making gravitational wave detectors a verdant field for work in quantum optics. The next generation of terrestrial gravitational wave detectors will be limited by near-field gravity–“Newtonian noise” from density waves in the surrounding environment. The ways forward will be to move underground (where this effect is smaller); measure, predict, and subtract the Newtonian noise contribution using a seismic sensor array; or to move into space.

Going into space makes feasible the use of extraordinarily long arms and yields complete freedom from terrestrial noise, allowing access to very low frequency gravitational waves. The Laser Interferometer Space Antenna (LISA) design is composed of three spacecraft forming an equilateral triangle, the whole constellation in solar orbit. These spacecraft will house truly inertial test-masses, floating within an internal vacuum enclosure while external microthrusters keep the spacecraft centered around the test mass. The gravitational wave channel is derived using time-delay interferometry. The proposed LISA design is sensitive to gravitational waves in the range 10^{-4} to 10^{-1} Hz (period of 3 hours down to 10 seconds).

1.8 This Dissertation

This dissertation describes modifications to the initial LIGO detectors that were undertaken between 2008 and 2010. The state of the LIGO detectors before these modifications is

described in [22] as well as numerous PhD dissertations, notably Rana Adhikari's [23] and Stefan Ballmer's [24]. Robert Ward's dissertation details the implementation and evaluation of DC readout at the LIGO 40 meter prototype interferometer in Pasadena [16].

In Chapter 2, I explain the principles and practice behind the sensitivity of the LIGO detectors. I show how the machine converts gravitational wave-induced phase modulation into a modulated optical field while offering a large amount of immunity to other effects.

In Chapter 3, I introduce two mechanisms of detecting this field and converting it to an electrical signal: homodyne and heterodyne detection.

Chapter 4 introduces the Output Mode Cleaner, its design and control, and the general idea of mode cleaners.

Finally, in Chapter 5, I present results demonstrating the performance of this system.

Chapter 2

The LIGO detector

In this chapter I explain how the LIGO detectors work.

2.1 Arms, cavities, etc

The purpose of the LIGO detectors is to measure the faint oscillations of spacetime imparted by far-away astrophysical processes. Through clever design and careful engineering, these machines are capable of resolving these tiny perturbations from the much louder sea of noise on the surface of the Earth.

As we have seen, a passing gravitational wave modulates the optical path length of light passing between inertial test masses. To exploit this effect and build a detector around it, we need to arrange to have inertial test masses. We need to be able to tell the difference between phase perturbations due to the gravitational wave and phase perturbations inflicted by our light source. We need to eliminate sources of phase variations that would be louder than the effect we wish to measure.

The essential points are:

- We approximate inertial test masses by hanging the optics as pendula. These act as inertial masses above the pendulum resonance.
- We build a Michelson interferometer for its common-mode noise rejection. This is nicely compatible with the tensor action of gravitational waves.
- To enhance the effect from a passing gravitational wave, we make the arms as long as possible. To further enhance the response, we have the light travel this path many times, by using resonant cavities.
- To increase the optical response to a gravitational wave, we increase the light power in the interferometer by using power recycling.

The following sections describe these principles in further detail.

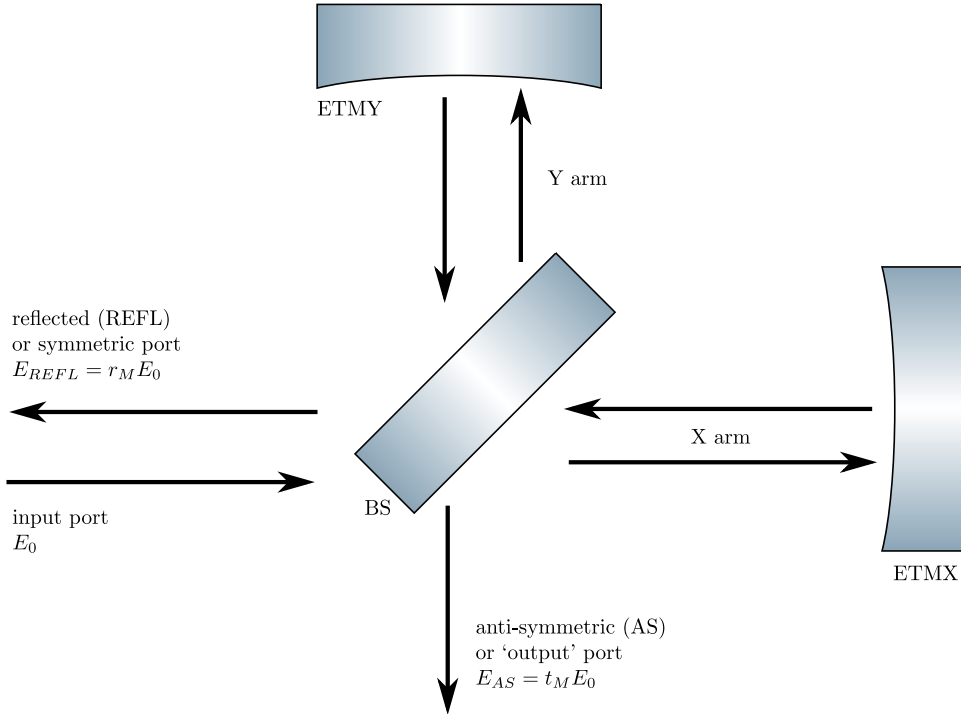


Figure 2.1: Michelson interferometer. This figure introduces some of the common nomenclature for the ports and optics of the Michelson interferometer. ETM stands for ‘end test mass.’

2.2 A Michelson

Contemplating the effect of a gravitational wave on a ring of test particles (figure 1.1), it is easy to imagine constructing a Michelson interferometer (figure 2.1) with its beamsplitter in the center of the circle and with two of the test particles forming the end mirrors of the Michelson. More importantly, the Michelson allows us to separate the differential motion of the two arms from the common motion, which is indistinguishable from laser frequency changes.

If we assume a perfect (lossless, 50/50) beamsplitter, the transmission and reflection coefficients for the Michelson are:

$$t_M = \frac{1}{2} (r_x \exp\{i2\phi_x\} - r_y \exp\{i2\phi_y\}) \quad (2.1)$$

$$r_M = \frac{1}{2} (r_x \exp\{i2\phi_x\} + r_y \exp\{i2\phi_y\}) \quad (2.2)$$

where $r_{\{x,y\}}$ are the amplitude reflectivities of the x- and y-arm mirrors, and $\phi_{\{x,y\}}$ are the phases accumulated as the light travels from the beamsplitter to end mirrors. It is useful

to change our variables to express these quantities in terms of the differential and common reflectivities and phases. Make the substitutions $\phi_x = (1/2)(\phi_+ + \phi_-)$, $\phi_y = (1/2)(\phi_+ - \phi_-)$ and $r_x = (1/2)(r_+ + r_-)$ and $r_y = (1/2)(r_+ - r_-)$:

$$t_M = \frac{1}{2}e^{i\phi_+} (r_+ i \sin \phi_- + r_- \cos \phi_-) \quad (2.3)$$

$$r_M = \frac{1}{2}e^{i\phi_+} (r_+ i \cos \phi_- + r_- \sin \phi_-) \quad (2.4)$$

The intent is for the arm reflectivities to be identical (so $r_- \rightarrow 0$), and to operate near the *dark fringe* ($\phi_- \rightarrow 0$) so that the input field does not couple directly to the output port (i.e. $t_M \rightarrow 0$). Given this configuration, there are two salient points concerning gravitational wave detection:

- Variations of the differential phase ϕ_- *linearly couple* to the *field amplitude* at the output port.
- Variations of the common phase ϕ_+ do not couple.

The field at the output port will thus be sensitive to suitably polarized gravitational waves but insensitive to laser frequency noise. (An orthogonally polarized gravitational wave, whose strain ellipse is rotated 45° , will modulate ϕ_+ but this detector sacrifices sensitivity to that polarization in order to gain common-mode noise immunity.)

Ultimately, we can not measure optical field amplitudes directly, but only the power, i.e. the envelope of the optical field, as the field itself oscillates at $c/(1064 \text{ nm}) \approx 300 \text{ THz}$, much too quickly to measure directly. We compute the power at the anti-symmetric and reflected ports by taking the squared magnitude of the field amplitudes. Using $P_{AS} = P_{BS} |t_M|^2$ and $P_{REFL} = P_{BS} |r_M|^2$:

$$P_{AS} = \frac{1}{4} P_{BS} (r_+^2 \sin^2 \phi_- + r_-^2 \cos^2 \phi_-) \quad (2.5)$$

$$P_{REFL} = \frac{1}{4} P_{BS} (r_+^2 \cos^2 \phi_- + r_-^2 \sin^2 \phi_-) \quad (2.6)$$

The power transmitted through the Michelson at the dark fringe is the *contrast defect*,

$$c_d = \frac{P_{AS}}{P_{BS}} = \frac{1}{4} (r_-)^2. \quad (2.7)$$

The linear relationship between ϕ_- and the electric field at the output port has turned into a quadratic relationship between ϕ_- and the output port power. We will turn to the task of recovering a linear signal in section 2.7, but first we will consider methods to magnify the effect of a gravitational wave on ϕ_- .

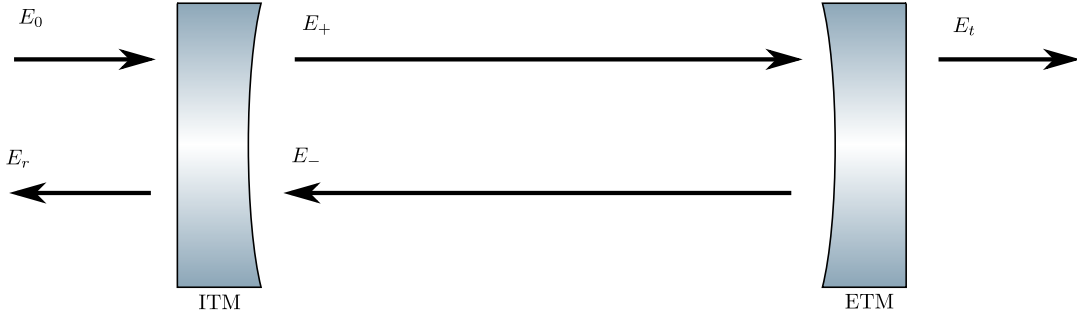


Figure 2.2: Fabry-Perot cavity. When used as an arm cavity, the two mirrors are known as the input (ITM) and end (ETM) test masses. Here E_0 indicates the amplitude of the incident electric field, E_r the reflected field, E_+ the forward-going intra-cavity field, etc.

2.3 Resonant cavities

One approach to increasing the phase imparted by the GW to the light in the arms of the interferometer would be to arrange for the light to make multiple traversals of the arm length. This could be in the form of a delay line (where the optical path makes several zig-zags down the arm length in a definite number of bounces), or a resonant cavity (made by facing two partially-transmissive mirrors at each other, resulting in an effective number of bounces). Resonant cavities were chosen for the LIGO arms. They appear in many other guises within the detector too, so the general theory is quite useful.

Consider the two-mirror system in Figure 2.2, a Fabry-Perot cavity. Light entering the cavity will interfere with light already circulating in the cavity. If, after making a round-trip through the interior of the cavity, the circulating light returns to its original phase (and spatial distribution), constructive interference will occur and the light will resonate in the cavity. If the mirrors have high reflectivity, then the light inside the cavity will survive for many round-trips inside the cavity. Any deviation from the required 2π radians of round-trip phase will be magnified on each bounce, making Fabry-Perot cavities extremely frequency-selective devices.

2.3.1 Fabry-Perot field equations

Here I will derive the basic properties of Fabry-Perot cavities, for simplicity ignoring the spatial distribution of light (which we will revisit in chapter 4), and its polarization. Despite these simplification, the results will have wide applicability.

We begin by writing down the relationships between the fields at each interface. For simplicity, we treat each mirror as a single (thin) interface. Let r_1 and t_1 be the amplitude reflectivity and transmissivity for the input mirror, and r_2 and t_2 describe the output mirror. I use the phase convention where transmission through a mirror conveys 90° of phase, i.e. a

factor of i in the amplitude:

$$E_+ = it_1 E_0 + r_1 E_- \quad (2.8)$$

$$E_- = r_2 e^{i2\phi} E_+ \quad (2.9)$$

$$E_t = it_2 e^{i\phi} E_+ \quad (2.10)$$

$$E_r = r_1 E_0 + it_1 E_1 \quad (2.11)$$

Solving these equations algebraically for E_r and E_t in terms of the incident field E_0 , we find the transmission and reflectivity of the cavity:

$$t_c \equiv \frac{E_t}{E_0} = \frac{-t_1 t_2 \exp i\phi}{1 - r_1 r_2 \exp i2\phi} \quad (2.12)$$

$$r_c \equiv \frac{E_r}{E_0} = \frac{r_1 - (r_1^2 + t_1^2) r_2 \exp i2\phi}{1 - r_1 r_2 \exp i2\phi} \quad (2.13)$$

where ϕ is the phase accumulated by the field as it travels from the first mirror to the second mirror. This phase depends on both the laser wavelength and the distance between the mirrors:¹

$$\phi = 2\pi\nu/\nu_0 \quad (2.14)$$

$$\nu_0 = c/(2L) \quad (2.15)$$

where $\nu = c/\lambda$ is the laser frequency, L is the cavity length, and ν_0 is the *free spectral range*, which describes the spacing between adjacent resonances.

2.3.2 the cavity pole

It is often useful to write the cavity reflectivity in the form of a rational transfer function,

$$r_c(s) = \prod_{n=-\infty}^{\infty} \frac{s - z_n}{s - p_n} \quad (2.16)$$

where $s = i\omega$. Substitute $\phi =$.

2.3.3 phase gain

For the arms of a gravitational wave detector, we set r_2 as close to unity as possible. We are interested in the phase of the reflected field.

Recall that the phase at frequency ω imparted by a pole at frequency ω_0 is $\tan^{-1}(-\omega/\omega_0)$; a zero at the same frequency subtracts this same phase. For a maximally over-coupled cavity

¹There is an additional contribution to the phase, the Guoy phase shift, due to geometric effects; this is described in chapter 4.

(i.e. with $r_2 = 1$), the cavity pole and cavity zero are equal and opposite, so contribute equal phase (\tan^{-1} is odd).

Changing the one-way phase of the arm by ϕ results in a phase change of

$$\phi_r = 2 \tan^{-1} \left(2f_{fsr} \frac{\phi}{\omega_0} \right) \quad (2.17)$$

where ω_0 is the cavity pole. Taking the derivative, we find the *phase gain*:

$$\frac{d\phi_r}{d\phi} = 2 \left[1 + \left(\frac{2f_{fsr}\phi}{\omega_0} \right)^2 \right]^{-1} \frac{2f_{fsr}}{\omega_0} \quad (2.18)$$

The phase gain on resonance is $2f_{fsr}/\omega_0 \approx 140$. This phase gain decreases as we detune the cavity further from resonance, but it is not seriously diminished until the cavity detuning approaches the cavity pole.

2.3.4 power buildup

2.3.5 coupling

2.4 Michelson with Fabry-Perot arms

To consider a Michelson interferometer with Fabry Perot cavities for arms, we can substitute the cavity reflectivity into our Michelson equations.

It is easier to simply put in the phase gain.

2.5 Power recycling

The Michelson interferometer tuned to a dark fringe for the laser carrier sends most of the laser power back towards the laser. Instead of discarding this power, it can be sent back into the Fabry-Perot Michelson interferometer. This is done by adding an additional mirror, the *power recycling mirror*, that forms a resonant cavity with the rest of the interferometer. Choosing the reflectivity of the power recycling mirror to match the effective reflectivity of the rest of the interferometer makes this cavity critically coupled; ideally all of the laser carrier is coupled into the interferometer and very little is reflected. Most of the light stays in the interferometer until it is lost to scattering or absorption.

2.6 The coupled cavity pole

We can consider the Fabry-Perot Michelson, or, really, any assembly of mirrors as a single compound mirror with a complex-valued, frequency-dependent reflectivity. In particular, we can model the power-recycled Fabry-Perot Michelson as a three mirror cavity.

The dynamics of three-mirror cavities are treated comprehensively in chapter 4 of Malik's thesis [25].

To find the transfer function of the coupled cavity, we can simply substitute the cavity reflectivity function $r_c(\phi)$ given in equation 2.13 into itself.

To find the cavity pole of the combined cavity, a good approximation results if we first compute the reflectivity of the shorter cavity on resonance, and substitute this into the expression for the cavity pole. We get:

$$f_{cc} \approx \frac{1}{2\pi} f_{fsr} \log \left(\frac{r_3 - r_1}{1 - r_1 r_3} r_2 \right) \quad (2.19)$$

2.7 Interferometer Sensing and Control

The laser light incident on the interferometer is phase-modulated at several frequencies, producing optical sidebands on the laser carrier. Light extracted from the interferometer at its various ports is incident on photodiodes; the photodiode signals are demodulated to produce signals.

[26]

2.8 Heterodyne detection

The initial LIGO detectors were designed to use, as much as possible, proven technologies. The proven technique for sensing the length/frequency mismatch of an optical cavity was the Pound-Drever-Hall (PDH) technique[27, 28], sometimes called reflection-locking, which can be used to lock the frequency of a laser to the length of a cavity, or vice versa.

In the basic PDH setup, the laser light incident on a resonant cavity is first phase-modulated at a frequency well outside of the bandwidth of the cavity, such that the sidebands are nearly anti-resonant in the cavity when the carrier is resonant. For small perturbations (in laser frequency or cavity length) around this point, the phase of the reflected carrier changes quickly, while the phase of the reflected sideband field changes more slowly. The reflected sideband field may therefore be used as a local oscillator by which to measure the carrier phase.

2.8.1 The Pound-Drever-Hall technique

The phase modulation may be expanded in terms of sidebands using the Jacobi-Anger expansion:²

$$\begin{aligned}\exp\{i\Gamma \cos \Omega t\} &= \sum_{n=-\infty}^{\infty} (i^n) J_n(\Gamma) \exp\{in\Omega t\} \\ \exp\{i\Gamma \sin \Omega t\} &= \sum_{n=-\infty}^{\infty} J_n(\Gamma) \exp\{in\Omega t\}\end{aligned}\quad (2.20)$$

Upon reflection from a cavity the phases of the carrier and the two sidebands will be rotated. This phase rotation converts the phase modulation to amplitude modulation, which is observed by the photodiodes. Typically, the carrier is held on resonance, where there is a very large change in reflected phase for a small change of detuning; the sidebands, on the other hand, are typically far from resonance and experience very little phase change.

The reflectivity of a lossless Fabry-Perot cavity is:

$$r_c = \frac{r_1 - r_2 \exp i2\phi}{1 - r_1 r_2 \exp i2\phi} \quad (2.21)$$

Suppose the carrier and upper and lower sidebands are incident upon this cavity, and the reflection from the cavity is incident on a photodiode. If the cavity length is L and the optical frequency is ν then $\phi = (2\pi)(L/c)\nu$. The sideband detunings are offset from this by $\pm(2\pi)(L/c)\Omega$. So, as a function of detuning, we have:

$$E_r = J_0 r_c(\phi) + J_1 r_c(\phi - (2\pi L/c)\Omega) + J_1 r_c(\phi + (2\pi L/c)\Omega) \quad (2.22)$$

2.9 Determination of LIGO cavity lengths and mirror reflectivities

The lengths of cavities and reflectivities of mirrors in LIGO are all driven by a small number of design decisions. This section is intended to be a brief and friendly derivation of some of these values. Definitive references are [29] or [26]; A more general reference is [22].

As in the preceeding sections, I simply use the plane-wave approximation for fields inside cavities. This introduces certain inaccuracies, as, for example, I ignore gouy phase. Nonetheless, comparison to the actual dimensions of LIGO shows good agreement.

It is useful to draw a distinction between macroscopic and microscopic lengths. Macroscopic lengths are those derived here and used in detector engineering, with magnitudes ranging from kilometers down to centimeters or millimeters. Microscopic lengths are those on the order of the wavelength of light and smaller, sometimes *much* smaller. Microscopic lengths are never determined explicitly; instead they are controlled by servo systems to hold cavities on resonance. When we say that a cavity is a certain macroscopic length, we retain the freedom to adjust the microscopic length to attain resonance.

²This expansion comes from the generating function $\exp\{\frac{1}{2}z(t-t^{-1})\} = \sum_{m=-\infty}^{\infty} t^m J_m(z)$ with $t = \exp\{i\omega t'\}$

Arm length

How big a detector can you build? The physical length of the detector sets the conversion between displacement and strain. Simply making the detector longer will make any fixed displacement noises into smaller strain noises-so we want the detector as large as possible. How big one can build is usually a result of geography, money, and politics. LIGO got

$$\boxed{L_+ = 4000 \text{ meters}} \quad (2.23)$$

The cavity length determines the free-spectral-range:

$$\nu_0 \equiv \frac{c}{2L_+} \approx 37.5 \text{ kHz} \quad (2.24)$$

Bandwidth

In the Fabry-Perot Michelson interferometer design, there is a trade-off between the detector's sensitivity and its bandwidth.³ As the storage time in the arm becomes longer and longer (either by making the arm longer, or by increasing its finesse), the sensitivity to gravitational waves increases commensurately. However, sensitivity to waves whose period is shorter than the storage time of the arm is attenuated. Thus there is a trade-off between sensitivity and bandwidth. One must choose a bandwidth. LIGO chooses:

$$f_c = 90 \text{ Hz} \quad (2.25)$$

Together, the free spectral range and the arm cavity pole determine the cavity finesse:

$$\mathcal{F} = \frac{f_{FSR}}{2f_c} \approx 210 \quad (2.26)$$

Test mass reflectivities

Knowing our desired finesse allows us to choose the mirror reflectivities. The finesse is uniquely determined by the fraction of circulating power that remains in the cavity after each roundtrip, which is given by a product of the mirror reflectivities and $r_L = \sqrt{1-L}$ where L represents losses due to scattering, absorption, etc.

$$\mathcal{F} \approx -\frac{\pi}{\log r_1 r_2 r_L} \quad (2.27)$$

This relation fixes the product $r_1 r_2$, leaving the ratio r_1/r_2 as a free parameter. This ratio determines the coupling of the cavity, from maximally over-coupled ($r_2 \rightarrow 1$), to critically

³Advanced LIGO will include an additional mirror, a *signal recycling mirror* at the output of the interferometer, forming an additional resonant cavity at the anti-symmetric port. This cavity allows the interferometer DC sensitivity to be increased without decreasing its bandwidth.

coupled ($r_1 = r_2$), or to cavity at all ($r_1 \rightarrow 1$). How do we choose the coupling? Intuitively, we want to couple as much light as possible into the cavity. In one point of view, this is so there is as much light as possible present inside the cavity to be phase modulated by the gravitational wave. The power gain inside the cavity is given by

$$g^2 = \frac{1 - r_1^2}{(1 - r_1 r_2)^2}$$

To maximize this, we want r_1 as small as possible, so we make the ETM as reflective as possible. It turns out that maximal over-coupling is the way to go. The best super-polished mirrors we could buy have transmissivities of 10 ppm, which gives

$$r_2 = \sqrt{1 - 10 \times 10^{-6}} \approx 0.999995 \quad (2.28)$$

Solving equation 1, we find:

$$r_1 \approx 0.985 \quad (2.29)$$

Power Recycling - Recycling Mirror

With the Fabry-Perot Michelson interferometer tuned to the dark fringe, all of the light not lost in the arm cavities is reflected back towards the laser source. To send this light back into the interferometer, we add a power recycling mirror, which forms a resonant cavity with the FP Michelson. We choose the reflectivity of the recycling mirror to make the cavity critically-coupled for the carrier.

With the Michelson on a dark fringe, the Michelson reflectivity is given by the cavity reflectivity on resonance:

$$r_c = \frac{r_1 - r_2 r_L}{1 - r_1 r_2 r_L} \quad (2.30)$$

where r_L represents losses in the arm cavity.

We choose:

$$r_{RM}^2 = 0.97 \quad (2.31)$$

The recycling mirror transmission is chosen to match the losses of the rest of the system.

Power Recycling - PRC cavity length

We need to have some radio-frequency sidebands in order to implement the heterodyne scheme that is used to control most of the interferometer. Its frequency is chosen to be several tens of MHz, and to be approximately⁴ anti-resonant in the arm cavities. We choose:

⁴If the sideband were perfectly anti-resonant in the arms, then the first harmonic would be resonant, which is undesirable.

$$f_{RF} \approx 24.5 \text{ MHz}$$

The RF sidebands must fit in the power recycling cavity. The resonant conditions for the carrier and for the sideband in the PRC are slightly different. Because the carrier is resonant in the (strongly over-coupled) arm cavities, it sees a sign flip in reflection from the arms that is not seen by the sideband. The carrier is actually *anti*-resonant in the PRC until the arms come into resonance and this extra sign flip comes into play. The minimum length of the PRC that satisfies this requirement occurs when the carrier accumulates π radians more phase than the lower sideband over a round-trip traversal of the cavity. (The upper sideband, in turn, acquires π radians more than the carrier, putting it 2π above the lower sideband, making them simultaneously resonant. The carrier gets its final π radians on reflection from the over-coupled arm.) Instead of relying on intuitive arguments, we can write down equations for the conditions of resonance:

$$\exp \{i(2l/c)\omega_0\} = -1 \quad (2.32)$$

$$\exp \{i(2l/c)(\omega_0 \pm \omega_{rf})\} = +1 \quad (2.33)$$

Solving these⁵, we find a nice relationship between the cavity length and the RF wavelength $\lambda_{rf} = c/f_{rf} \approx 12$ meters:

$$2l_+ = \lambda_{rf} \left(m + \frac{1}{2} \right)$$

where m is any integer. The length corresponding to $m = 0$ is inconveniently short⁶, so we choose $m = 1$, giving a power recycling cavity length of:

$$\boxed{l_+ = 9.18 \text{ meters}}$$

The PRC length is set to allow simultaneous resonance of the carrier and sidebands in the power recycling cavity.

Schnupp asymmetry

Now that we have the RF sidebands resonant in the recycling cavity, we need to get them to the output port.

A Michelson with identical arms has no frequency selectivity; in principle even white light would experience bright and dark fringes. Introducing an offset breaks this degeneracy, as the offset allows higher frequency waves to accumulate more phase than slower frequencies. Introducing a macroscopic difference in the arm lengths separates the carrier fringes from the sideband fringes. In the longer arm, now, the lower sideband accumulates less phase

⁵Remember the multivaluedness of the logarithm, i.e. $\log 1 = i2\pi n$ for all integers n .

⁶I assume this is the reason...

than the carrier, and the upper sideband accumulates a bit more. When the beams from the two arms recombine, the phase difference now depends on the frequency. With such an asymmetry, the Michelson can be simultaneously reflective of the carrier and partially transmissive of the sidebands.

How much sideband transmission do we need? The Michelson is acting as the second mirror in a resonant cavity. If we want to have perfect transmission of the sideband to the output port, then the power recycling cavity must be critically coupled for the sideband. This occurs when the Michelson transmission of the sideband is equal to the transmissivity of the RM. This scheme for getting the sideband to the “dark” port is attributed to Lisa Schnupp, and the offset is called the Schnupp asymmetry.

The Michelson reflectivity for the sideband is:

$$r_M = \cos \frac{2\pi f_{rf} l_-}{c} \quad (2.34)$$

(The fringe of the lower sideband lags that of the carrier, and the upper sideband leads the carrier. But because the carrier itself is on a dark fringe, the transmission of both the upper and lower sidebands turns out to be the same.)

Solving $r_M^2 = 0.97$ in order to match the RM, we find a Schnupp asymmetry of

$$l_- = 34 \text{ cm} \quad (2.35)$$

The Schnupp asymmetry sets the coupling of the RF sidebands to the antisymmetric port.

2.10 Heterodyne shot noise

I conclude this chapter with a discussion of the shot-noise-limited sensitivity of a detector using heterodyne readout.

When a constant optical power P is incident upon a photodetector, we expect to observe Poisson shot noise in the resulting photocurrent. This shot noise has a white (flat) power spectrum, with amplitude spectral density $\sqrt{2P\hbar\nu}$, where $\hbar\nu$ is the energy of an individual photon.

In the heterodyne readout system, the power on the photodiode is *not* constant; instead, the power varies sinusoidally at a frequency $2f_{mod}$ due to the beat between the upper and lower RF sidebands. At any given instant, a measurement of the rate of photon arrival will return a value from the Poisson distribution with mean $P/(\hbar\nu)$, which has standard deviation $\sqrt{P/(\hbar\nu)}$. A measurement of power therefore will give $P \pm \sqrt{\hbar\nu P}$, where P is varying sinusoidally with time. This is an example of cyclostationary noise; a sample realization is depicted in figure 2.3. When considering a long time series ($t \gg 1/f_{mod}$), the signal will appear to have a noise floor determined by its average power. On closer examination, however, we see that the noise comes in bursts.

The bursty nature of this noise becomes a problem when we consider demodulation. Comparing the demodulation waveforms ($\cos 2\pi f_{mod}t$ and $\sin 2\pi f_{mod}t$) to the envelope of the

noise, we see that one demodulation quadrature systematically samples the highest variance portions of the timeseries, while the other quadrature samples the lowest variance portions (see figure 2.3). The result[30] is that the shot noise ASD in a demodulated signal is

$$\sqrt{2h\nu\bar{P}\left(\frac{1}{2} - \frac{1}{4}\cos 2\theta\right)} \quad (2.36)$$

where \bar{P} is the average power on the photodiode and θ is the demodulation phase.

The shot noise level in a heterodyne readout is a more subtle matter, as illustrated by the number of publications on the topic: [30, 31, 32, 33, 34]

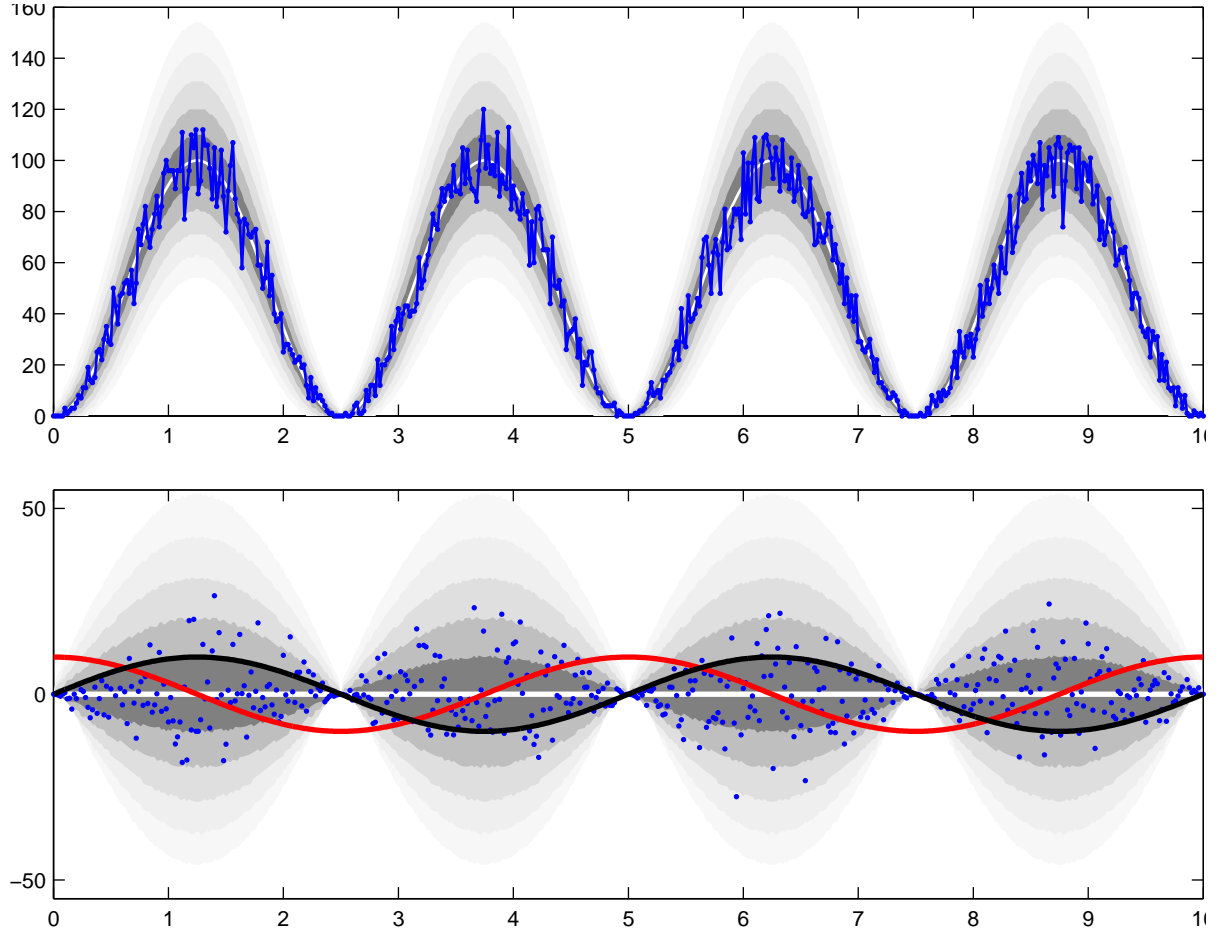


Figure 2.3: **(a)** Model of shot noise in the presence of sinusoidal power modulation, as occurs in optical heterodyne detection. The photodiode sees a power modulation at $2f_{mod}$ (white) due to the beat between the upper and lower modulation sidebands at $f_{carrier} \pm f_{mod}$. The gray levels represent the $1\sigma, 2\sigma, \dots, 5\sigma$ ranges for a Poisson distribution. The blue dots are a sample realization of this noise. **(b)** Subtracting the mean from (a) leaves only the noise; its bursty nature is obvious. Shown in black and red are the I and Q demodulation waveforms, respectively. It is clear that the in-phase demodulation (I) samples regions of the time series with higher variance than the quadrature phase (Q). This leads to a higher variance (shot noise level) in the I signal and a lower one in the Q signal relative to what one would expect from a naïve assumption based on the average power considered over a whole period of the waveform.

Chapter 3

DC Readout

The initial LIGO detectors used RF heterodyne detection, inspired by the Pound-Drever-Hall technique, to sense all interferometer length degrees of freedom and most angular degrees of freedom. During Enhanced LIGO, the sensing of the gravitational wave channel (DARM) was changed to a form of homodyne detection called DC readout. In this chapter I explain the motivation for and theory behind DC readout.

3.1 Principle of DC readout

A homodyne readout system differs from a heterodyne system by using a local oscillator at the same (optical) frequency as the field we wish to measure. In DC readout we bring this

DC readout creates a homodyne local oscillator by putting a small offset into the Michelson or DARM degree of freedom, moving the interferometer slightly off of the DARM fringe at DC. In this “fringe” view, the operation is very simple to understand: moving off of the null point introduces a non-zero first derivative.

The true beauty of this technique is that it exploits the filtering action of the compound interferometer to produce the local oscillator; any fluctuations in the amplitude or frequency of the input laser field are attenuated by the coupled cavity pole before reaching the output port.

3.2 Motivation for DC readout

Some of the motivations of DC readout and an output mode cleaner are:

- The filtering action of the compound interferometer produces an extremely quiet local oscillator. This reduces the coupling of laser noises to the readout.
- Contributions from noise on the electronic oscillator used to create the RF sidebands are greatly reduced.

- The shot-noise-limited sensitivity of homodyne detection is inherently better than that of heterodyne detection, for a fixed amount of power on the detection photodiodes, by a factor of at least $\sqrt{3/2}$.
- The shot noise level may be further reduced through the injection of squeezed quantum vacuum. This is much more technically feasible with homodyne detection than heterodyne detection. This has recently been demonstrated at the GEO600 detector and a prototype implementation is underway at Hanford.
- In DC readout, the signal field and the local oscillator are guaranteed to have perfect spatial overlap, since they come from the same place. By contrast, in the conventional heterodyne arrangement, the RF fields and the carrier are resonant in different cavities and may occupy slightly different spatial modes. This leads to a reduction of shot-noise-limited SNR. (However, an output mode cleaner can be used to force good overlap in either case.)
- The output mode cleaner greatly decreases the amount of power that must be detected by the detection photodiodes by removing spurious higher order modes.

3.2.1 Calculation of the optical gain

To the extent that the introduction of DC offset simply creates a nonzero carrier field at the output port and does not otherwise affect the interferometer dynamics, the frequency response of the interferometer is the same in DC readout as in heterodyne readout, except for an overall scaling. This can be seen by considering the sideband picture (see Figure 3.1) and is borne out by the following derivation.

The optical gain for slow variations of the differential arm length can be found by calculating the power at the output port as a function of differential arm displacement and taking the derivative. The frequency response within the detection band is put in by hand. (Is there a nice way to do this in a frequency-dependent manner?)

The amplitude transmission coefficient of a Michelson interferometer is:

$$t_M = \frac{1}{2} (r_x(\phi_x) - r_y(\phi_y)) \quad (3.1)$$

where r_x and r_y are the amplitude reflectivity coefficients of the arms with detunings ϕ_x and ϕ_y .

We adopt a change of variable $\phi_- = \phi_x - \phi_y$, $\phi_+ = \frac{1}{2}(\phi_x + \phi_y)$.

For an interferometer with perfectly reflective arms, we have

$$t_M = \frac{1}{2} (e^{i\phi_x} - e^{i\phi_y}) = \frac{1}{2} (e^{+i\phi/2} - e^{-i\phi/2}) = i \sin \frac{\phi_-}{2} \quad (3.2)$$

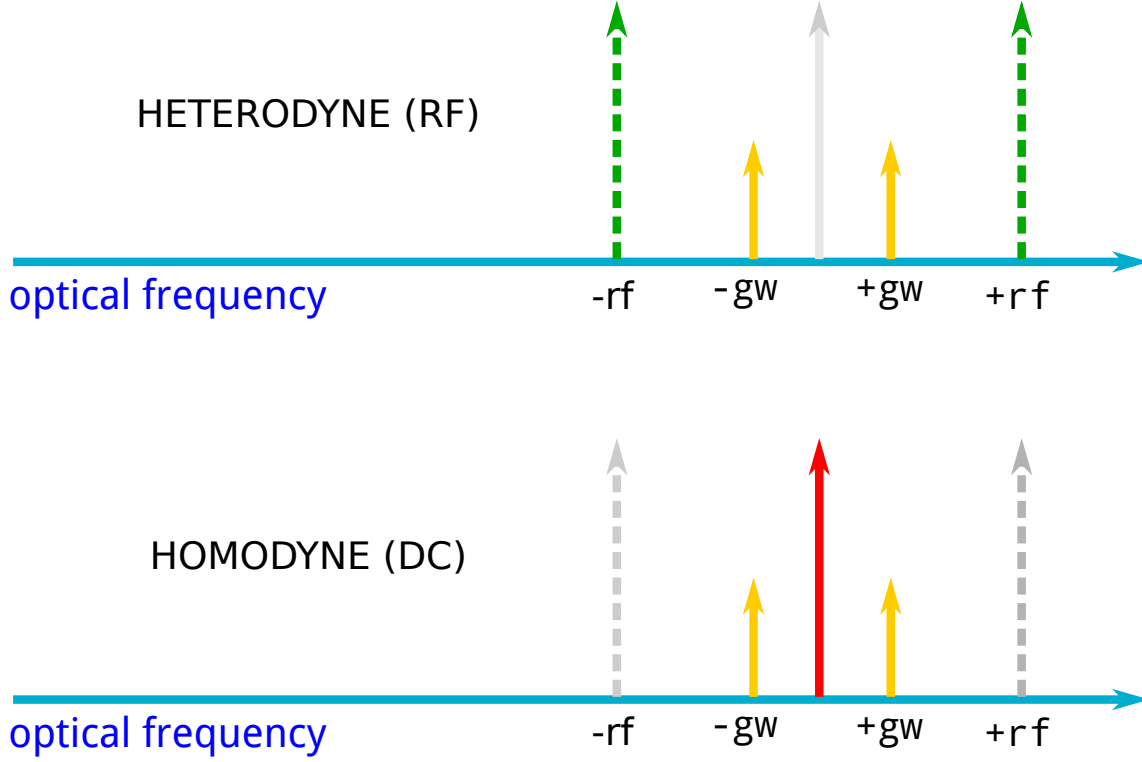


Figure 3.1: Depiction of the fields in DC and RF readouts. (a) In RF readout, the laser carrier is suppressed by operating the Michelson on a dark fringe for the carrier. Differential phase modulation in the arms becomes amplitude modulation of the (suppressed) carrier, depicted as the audio-frequency sidebands at $\pm f_{gw}$. The photodiode sees a beat between the GW signal and the RF sidebands. In homodyne readout, a carrier-frequency local oscillator is introduced—in DC readout this is done by introducing a microscopic asymmetry between the two arms. The RF sidebands are no longer needed and are removed by the output mode cleaner. The GW-induced sidebands appear as amplitude modulation on the carrier, which is sensed directly by the photodiodes.

The power at the output port is

$$P_{AS} = P_{BS} \sin^2 \left(\frac{\phi_-}{2} \right) \quad (3.3)$$

The differential phase is equal to the wavenumber $k = (2\pi)/\lambda$ multiplied by the differential displacement x multiplied by the phase gain of the cavity and an additional factor of two, since a simple displacement of an end mirror causes $2x$ path length change. For a cavity with amplitude reflectivity $r_c(\phi)$, this phase multiplier is:

$$M(\phi) = \text{Im} \frac{1}{r_c(\phi)} \frac{\partial}{\partial \phi} r_c(\phi) = \text{Im} \frac{r'_c}{r_c}$$

giving:

$$\phi_- = 2kMx_-$$

So the output power is

$$P_{AS} = P_{BS} \sin^2 kMx_- \quad (3.4)$$

The optical gain at for slow differential motion is simply the derivative of P_{AS} . Here we assume that the change of P_{BS} and the phase gain M are negligible:

$$S_{DC} = \frac{dP_{AS}}{dx_-} = P_{BS} 2kM \cos() \sin() \quad (3.5)$$

For convenience we can write this in terms of P_{AS} :

$$S_{DC} = 2\sqrt{P_{BS}P_{AS}}Mk \cos(kMx_-) \quad (3.6)$$

The cosine term is very near unity and can be neglected. We write the power at the beam-splitter in terms of the carrier amplitude recycling gain g_{CR} and the power at the input to the interferometer: $P_{BS} = g_{CR}^2 P_{IN}$. So we get:

$$S_{DC} = 2\sqrt{P_{IN}P_{AS}g_{CR}}(\Delta x)M(k\Delta x + \omega) \quad (3.7)$$

Figure ?? compares this analytic expression to results obtained via a numerical modelling with Optickle. Agreement within the LIGO detection band is excellent.

Better expression for P_{AS}

We can substitute $\phi = \phi_x = -\phi_y$ since we're interested in differential motion of the arms, and substitute the Fabry-Perot reflection coefficient:

$$r_c(\phi) = \frac{r_1 - r_2 e^{i2\phi}}{1 - r_1 r_2 e^{i2\phi}} \quad (3.8)$$

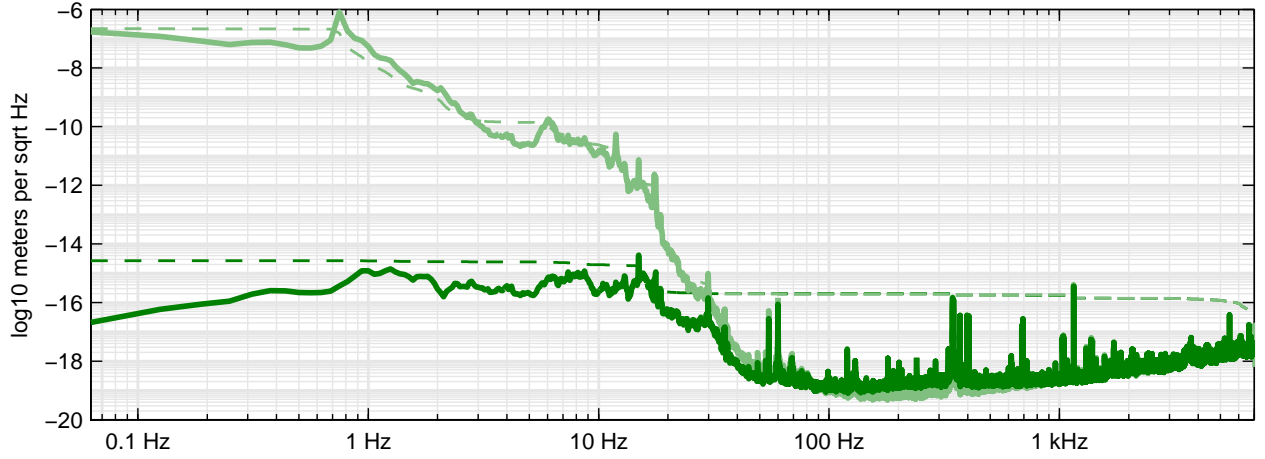


Figure 3.2: Residual DARM

where $\phi = kx$ is the one-way phase accumulated in the arm, r_1 is the reflectivity of the ITM, and r_2 is the reflectivity of the ETM.

Working out t_M for differential arm displacement, we find:

$$t_M = ir_2 g^2 \frac{\sin 2\phi}{1 + F \sin^2 \phi} \quad (3.9)$$

where g is the amplitude gain of the arm cavities and F is their coefficient of finesse. Taking the modulus-squared of this, and then multiplying by the incident power, we get the power at the output port:

$$P_{AS}(\phi) = P_{BS}(\phi) R_2 \frac{g^4}{(1 + F \sin^2 \phi)^2} \sin \phi \cos \phi \quad (3.10)$$

[steps omitted]

Taking the derivative with respect to δx , we find the optical gain, in Watts/meter, as:

$$S_{DC} \approx 2\sqrt{P_{IN} P_{AS} g_{cr} r_{cp} k} \quad (3.11)$$

3.3 Offset

As long as the DARM offset is sufficiently small, the degradation of power recycling is negligible.

Optical gain and shot noise level both scale like the square root of the power at the detection port (for small offsets). Thus the detection SNR is relatively insensitive to the particular offset.

3.3.1 Decrease in arm power due to off-resonance operation

The decrease in buildup for a cavity operated off-resonance goes like $(2\mathcal{F}/\pi)^2\phi^2$, where ϕ is the cavity detuning. For $\mathcal{F} = 220$ and $\phi = (2\pi/1064 \text{ nm})(10 \text{ pm})$, the fractional power loss is only 7×10^{-5} .

3.3.2 Decrease in power recycling gain due to power loss at the output port

Chapter 4

Output Mode Cleaner

4.1 Introduction

Any fields present on the detection photodiode other than the signal field and the local oscillator will lead to additional shot noise but no additional signal: a degradation of SNR. The additional fields can be either distinct in frequency or in spatial mode.

To remove these spurious fields, we employ an optical filter cavity at the interferometer's output. This is the *output mode cleaner* (OMC).

4.2 General theory of mode cleaners

Critically-coupled resonant cavities act as optical filters, allowing the resonant mode to be transmitted while all orthogonal modes are highly attenuated. These cavities can be not only frequency-selective, but also select a single spatial mode.

Gaussian beams and higher-order modes accumulate phase slightly faster than plane waves. The extra phase (beyond the $\phi = kz$ expected for a plane wave) is the Guoy phase. It accumulates most rapidly as a beam goes through a focus (waist). A Gaussian beam accumulates 180° as one moves from $z = -\infty$ to $z = +\infty$ through the waist; a higher-order Hermite Gauss mode accumulates more. The Guoy phase shift as a function of beam axis coordinate is given by

$$\phi_g(z) = (1 + n + m) \tan^{-1} \left(\frac{z - z_0}{z_R} \right) \quad (4.1)$$

where z is the coordinate along the beam axis, z_0 is the location of the waist, z_R is the Rayleigh range of the beam, and n and m are the mode indices of the Hermite Gauss mode.

A two-mirror symmetric cavity of length L with mirrors of radius of curvature R has a g -factor of $g = 1 - L/R$; from this we can calculate the Rayleigh range of the mode in the cavity:

$$z_R = \frac{L}{2} \sqrt{\frac{1+g}{1-g}} \quad (4.2)$$

$$\phi_n^{cav} = (n + 1/2) (\tan^{-1}(L/2)/z_R - \tan^{-1}(-L/2)/z_R) \quad (4.3)$$

$$= (n + 1/2) \cos^{-1} g \quad (4.4)$$

The higher order modes have the same wavefront curvature as the lowest order gaussian mode. They differ only in experiencing the extra Guoy phase. The result is that higher order modes resonate at a slightly different (shorter) cavity length than the fundamental mode of the same frequency.

For resonance to occur, the total phase shift from one mirror to the other, including both the plane wave propagation phase $kL = \pi\nu/\nu_0$ and the Guoy phase shift, must be a multiple of π (so that the roundtrip phase is a multiple of 2π):

$$kL - 2(m + n + 1) \cos^{-1} g = \pi(q + 1), \quad q \in \mathbb{Z} \quad (4.5)$$

For the special case of $L = 2z_R$, the increase in the Guoy phase as m or n is increased is exactly π radians. For this special case—a *confocal cavity*—all of the spatial modes at a given frequency resonate simultaneously. For a mode cleaner cavity, we want precisely the opposite; we will carefully choose the cavity geometry to separate higher-order spatial modes from the fundamental mode of the laser carrier.

We can express the additional Guoy phase shift of higher order modes as an equivalent frequency shift that would allow them to resonate at the same cavity length as the carrier. The effective frequency shift is

$$\Delta\nu = \frac{2}{\pi} \nu_0 \cos^{-1} g \quad (4.6)$$

where ν_0 is the free spectral range.

4.3 Eigenmodes

A phase-front that returns to its original state after making a round-trip through the optical cavity will interfere constructively with itself, resonating in the cavity. The set of such amplitude distributions which are stable in the cavity and do not mix with one another are collectively the *eigenmodes* of the cavity. The eigenmodes of a cavity made with spherical mirrors are parametrized by either the Hermite-Gauss or Laguerre Gauss modes. (The same functions also describe the energy eigenfunctions of the quantum harmonic oscillator.)

The Hermite-Gauss modes are given by:

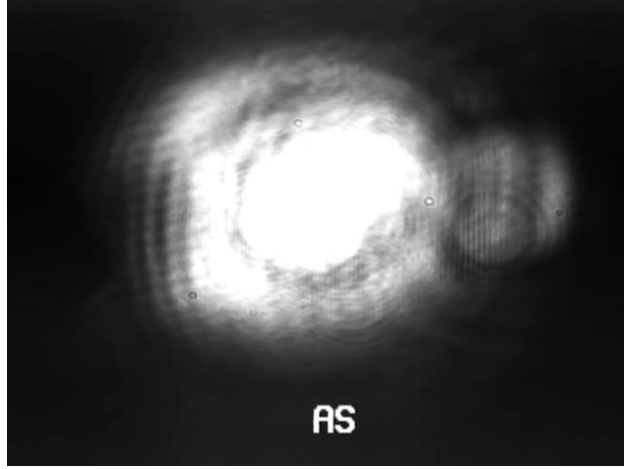


Figure 4.1: Image of the beam spot at the output port taken using a CCD camera. Although this image is saturated in the central portion, it shows the messy junk light surrounding the central gaussian beam. This includes contributions from both the carrier and the 25 MHz sidebands.

$$E_{nm}(x, y) = E_0 \sqrt{\frac{2}{\pi w n! m! 2^n 2^m}} \exp \left\{ -\frac{x^2 + y^2}{w^2} \right\} H_m \left(\frac{\sqrt{2}x}{w} \right) H_n \left(\frac{\sqrt{2}y}{w} \right) \quad (4.7)$$

4.4 Physical design of the cavity

The output mode cleaner (OMC) consists of a four-mirror bowtie cavity with a finesse of approximately 350. The cavity optics and detection photodiodes are attached to tombstones which are bonded to a glass slab. This entire optical bench is suspended by a double pendulum, which in turn rests on an active seismic isolation platform, all of which is contained within the vacuum envelope. For convenience the chamber containing the OMC is isolated from the rest of the LIGO vacuum envelope via a septum window, allowing the independent venting of this chamber for easier access.

The output of the OMC is split via a 50/50 beamsplitter and directed onto two high-quantum-efficiency InGaAs photodiodes. The two photodiode signals allow the formation of sum and difference signals, the difference providing a diagnostic ‘nullstream’.

4.5 Requirements

The OMC is required to sufficiently filter the light present at the output port such that contributions from the RF sidebands and higher-order spatial modes become negligible. To

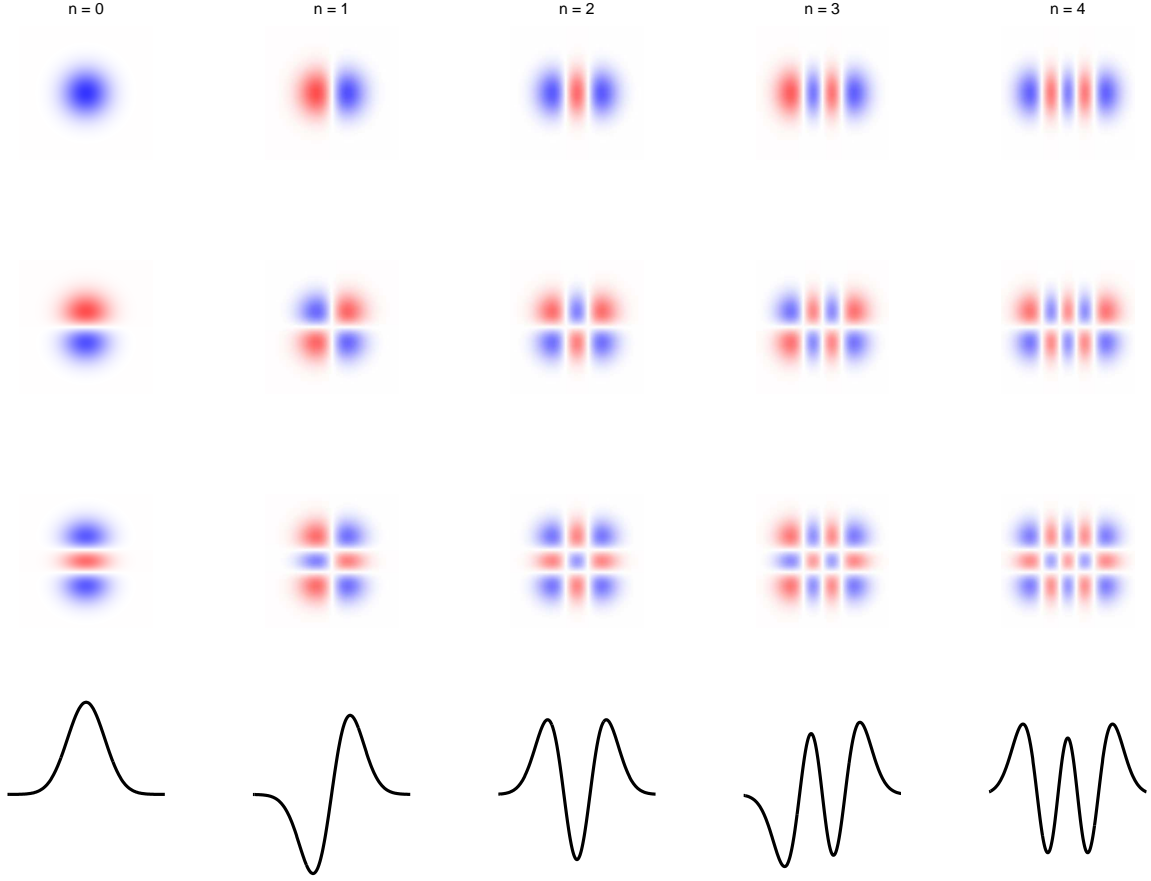


Figure 4.2: Hermite-Gauss modes. Positive amplitude is indicated in red and negative amplitude in blue.

parameter	design	H1	L1	units
perimeter (p)	1.042	1.077	1.016	m
beam waist (w)	477	496	463	μm
Finesse (\mathcal{F})	400	360	360	
FSR	287.7	278.3	295.2	MHz
cavity pole	360	390	410	kHz
g-factor	0.739	0.725	0.722	
HOM freq shift	69.4	67.2	71.8	MHz
transmission	1	≥ 0.95	≥ 0.90	

Table 4.1: Designed and measured properties of the Hanford and Livingston output mode cleaners.

exclude the RF sidebands, the cavity length is chosen such that the RF sideband frequencies are anti-resonant in the cavity, which yields minimum transmission.

4.6 Choosing the OMC finesse

All things being equal, we want the best possible filtering capability from the OMC.

The transmission of a lossless critically-coupled cavity is given by

$$T = \frac{1}{1 + \frac{4}{\pi^2} \mathcal{F}^2 \sin^2 \phi} \quad (4.8)$$

where \mathcal{F} is the cavity finesse and ϕ is the cavity's detuning from resonance. Since the cavity will be locked to resonance for the laser carrier, to find the attenuation of other modes, we set ϕ to the detuning of these modes.

The maximum attenuation of a mode is given by $(4/\pi^2)\mathcal{F}^2$.

After filtering by the OMC, we want the shot noise contributions from unneeded modes to be negligible, and the contribution from noises on these fields to also be negligible. Almost any cavity would be sufficient to reduce excess shot noise contributions. The need for a high finesse OMC comes from the need to eliminate audio frequency noises carried on the RF sidebands and higher-order spatial modes.

Consider the contribution of intensity noise on the RF sidebands. Any residual intensity noise on the RF sidebands will contribute directly to the DC readout signal. Assume that the carrier has about 100 mW power and that the RF sidebands have about the same amount of power, and assume that the laser intensity noise is 10^{-7} RIN. The shot noise RIN on 100 mW is (per equation 7.20) $\sqrt{2h\nu/P} \approx 2 \times 10^{-9}$. Thus we need to attenuate the RF sidebands by at least a factor of 100.

The RF sidebands will not be exactly anti-resonant in the cavity but will actually lie at about $0.1f_{sr}$ away from the carrier. Thus the attenuation is diminished by approximately $\sin^{-2}(0.1\pi) \approx 10$. So we need attenuation of 1000. But we really want at least a factor of 10 margin, so we'll want maximum attenuation of 10000. This means we need a finesse of at least 160.

4.7 Length control (LSC)

The cavity length must be controlled to maintain the resonance of the laser carrier. To sense the mismatch between the laser carrier and the cavity length, we modulate the cavity length by a small displacement at high (audio) frequency and monitor the transmitted light intensity for a signal at the same frequency. Cavity transmission is a quadratic function of the frequency/length mismatch; if the modulation is perfectly symmetric around the point of peak transmission, there will be no linear coupling. Effectively, we sense the first derivative of the transmission with respect to cavity length.

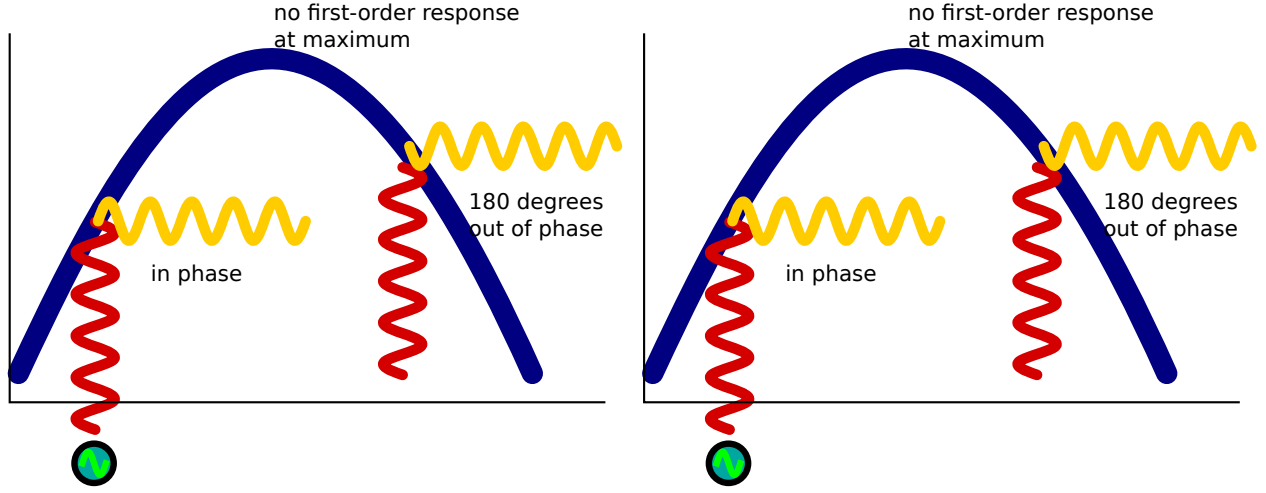


Figure 4.3: Cartoon view of dither locking

Modeling the dither locking

Suppose $f(x)$ is a function we wish to maximize; in this case, f gives the power transmitted through the OMC as a function of length offset. We let $x = x_0 + A \cos \omega t$, where A is the amplitude of the dither and ω is its frequency. We can expand f as a power series around x_0 :

$$f(x) \approx f(x_0) + f'(x_0)(x - x_0) + f''(x_0)(x - x_0)^2 + \dots \quad (4.9)$$

$$\approx f(x_0) + f'(x_0)A \cos \omega t + f''(x_0)A^2 \cos^2 \omega t + \dots \quad (4.10)$$

The amplitude of the $\cos \omega t$ term is proportional to the first derivative of f at the current operating point. (There are also contributions from higher derivatives, but we assume the lower derivatives dominate.)

Noise limits

Suppose the OMC has coefficient of finesse F and P watts on the photodiode. The dither amplitude is A and dither frequency is ω . What is the sensing noise limit?

The background is Gaussian white shot noise, equally distributed into the two demodulation quadratures. So the noise floor of the demodulated signal is $(1/\sqrt{2})\sqrt{2h\nu P}$.

The transmission of the OMC goes like $T(x) = 1/(1 + Fx^2)$ which has first derivative $T'(x) = -2Fx/(1 + Fx^2)^2 = -2Fx + O(x^3)$. Thus the optical gain is $-2FA$ watts per meter.

The fast PZT actuator is dithered at 10 kHz and this signal is synchronously demodulated in the transmitted light. The bandwidth of the servo is about 100 Hz.

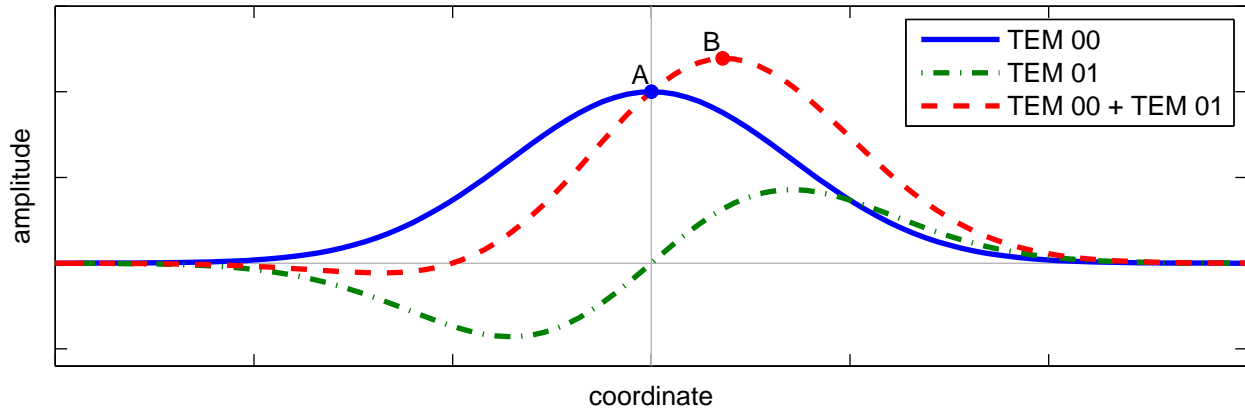


Figure 4.4: The sum of a gaussian and a first-order higher order mode resembles a displaced gaussian. A basic dither alignment scheme, which maximizes the power transmitted through the OMC, would operate near point B, rather than point A.

4.8 Input beam control (ASC)

In addition to controlling the cavity length to keep the carrier resonant, we must control the pointing of the beam incident on the OMC.

The decomposition of a given optical field into Hermite-Gauss eigenmodes is dependent upon a choice of origin and spot size. The OMC cavity will select the projection of the incident field onto its eigenmode. The optics directing the interferometer output beam to the OMC

Aligning the input beam to the OMC is a significant problem. The OMC can only clean the mode insofar as we can identify the mode we want to keep.

Several OMC alignment schemes were implemented and utilized.

The simplest alignment control simply uses the two QPDs mounted on the OMC breadboard. This has the advantage of being very robust and not requiring that the OMC already be locked, and so it is ideal for initial alignment of the OMC before locking the cavity. The QPD alignment, however, has no notion of the ideal DC pointing of the beam and is sensitive not just to the carrier, but also the RF sidebands.

A second alignment scheme is to dither the two steering mirrors each in pitch and yaw, demodulate the OMC transmitted signal at these frequencies, and feed back to the mirrors. This produces an alignment system which maximizes power transmitted through the OMC. Because this is a quadratic point, linear beam jitter coupling is nulled.

Junk light, however, will lead the dither alignment astray.

RF Wavefront sensing. We did not really consider this.

AF IM WFS. The same OMC length dither which is used to lock the cavity length produces an audio-frequency sidebands of the OMC mode in reflection. The beats between this light and the light rejected from the OMC on a pair of photodiodes can be used to produce alignment error signals.

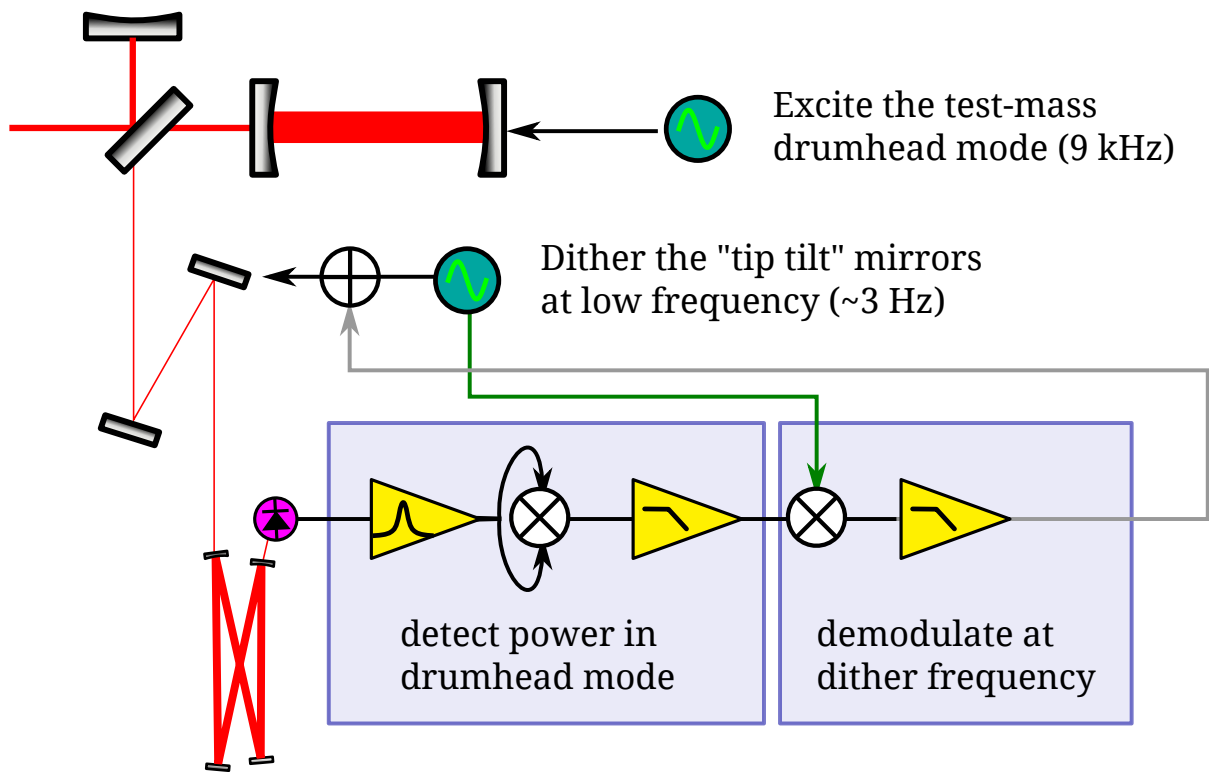


Figure 4.5: Drumhead dither

Beacon dither.

SNR dither. Nicolas’s scheme.

4.9 Automatic gain control

The optical gain of the interferometer naturally varies slowly as alignment drifts and the thermal state of the mirrors changes. The over-all loop gain must be kept within a few dB of its nominal value in order for the loop to remain stable.

Before S6 this was done by periodically running a script which measured the loop gain and adjusted a digital gain to bring it to nominal.

The flexibility of the realtime code generator allowed us to implement an automatic gain control servo directly in the OMC front-end. This was a nice convenience.

4.10 Residual fluctuations

4.11 Optical characterization

4.11.1 Mode scan

With the interferometer controlled using the heterodyne readout, the Output Mode Cleaner can be used as a mode analyzer cavity by varying the cavity length by at least a free-spectral-range. Because this range is more than the fast PZT actuator, this is accomplished by putting a large step into the thermal actuator.

4.11.2 Scattering

From the output port, the interferometer appears almost perfectly reflective. Any light scattered by the output optics at a small angle could scatter into the interferometer mode, reflect off of the interferometer, and interfere with the other fields there.

4.12 Interferometer lock acquisition

Initial lock acquisition of the Enhanced LIGO interferometers is the same as in Initial LIGO[35]. Once the interferometer is locked using the heterodyne readout schemes, a DARM offset is introduced to allow carrier light to be transmitted to the output port. The Output Mode Cleaner is then locked to this carrier light. Once the OMC is locked to the carrier, control of DARM is transferred to the DC readout system. After this transition, a few other changes are made to engage the OMC alignment servoes and to put the readout electronics into low noise mode. At this point the interferometer has reached its operation configuration and astrophysical data-taking (“science mode”) begins.

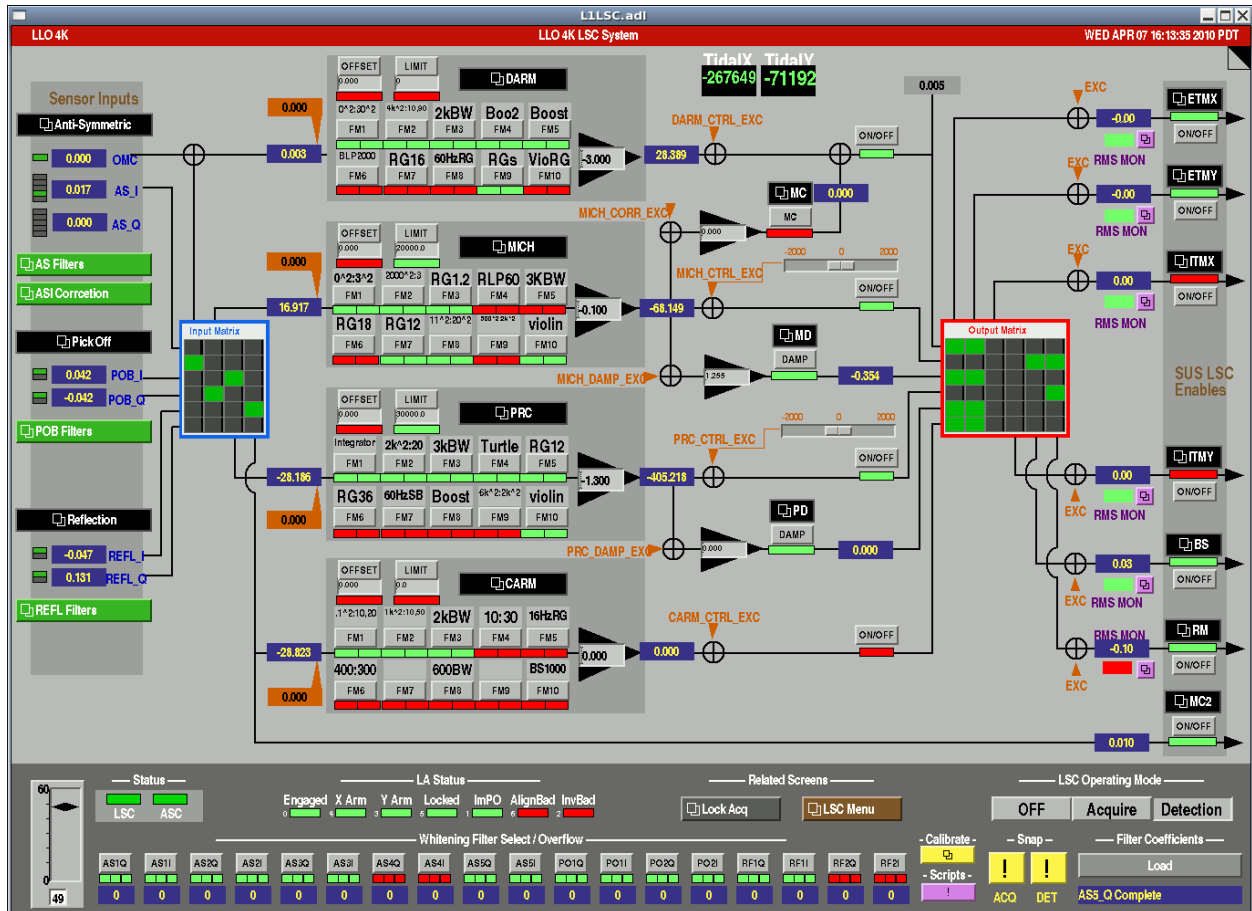


Figure 4.6: The control screen for the Length Sensing and Control subsystem at Livingston. The control screen depicts signal flow in a generally left-to-right manner. Photodiodes at the anti-symmetric (AS), pick-off (PO), and reflected (REFL) ports are indicated on the extreme left. These signals are combined via an input matrix to form the DARM, MICH, PRC, and CARM degrees of freedom. These signals are processed through an array of filter banks defining the control filters. Finally, the signals pass through an output matrix and are then directed to the individual optics.

4.13 Beam diverter

When the interferometer loses lock, the stored power must be dumped somewhere. Typically, due to the presence of the power recycling mirror, the stored power comes out the output port. This high-power transient is sufficiently strong to burn the detection photodiodes. In order to prevent this, one of the steering mirrors is used as a fast shutter. It is able to zero the transmission through the OMC in approx 2 ms.

4.14 The Front End

Be exhorted: you really can predict the noise floor accurately—to accept a noisy front end is one of the stupidest and most expensive mistakes you can make in designing sensitive optical instruments. Measure it, and make sure you can explain every half decibel. – Phil Hobbs, *Building Electro-Optical Systems* [36]

Chapter 5

DC readout performance and noise couplings

The coupling of noises from the laser source and RF oscillators to the gravitational wave readout channel differ considerably in RF and DC readouts. In addition, DC readout with an OMC is generally much more sensitive to beam motion (jitter). These couplings are of primary interest in designing the optical readout of a gravitational wave detector.

Furthermore we should verify that the touted sensitivity improvements of DC readout are realized.

In this chapter, I will sketch the technique for calculating expected noise couplings analytically and numerically, and I will present measurements of these noise coupling measurements made on the two Enhanced LIGO interferometers.

5.1 Sensitivity

The primary figure of merit of a gravitational wave detector is its noise floor, calibrated as a strain spectral density. When evaluating DC readout in Enhanced LIGO, we can begin by looking at the noise floor: was the promised sensitivity delivered? For the readout, the answer is a resounding yes. Given the input power and other known parameters of the interferometer, the noise floor is accurately modeled.

The shot-noise-limited sensitivity of a power-recycled interferometer is given by a small number of parameters:

- the length of the arm cavities ($L = 3995$ m)
or, equivalently, the free spectral range ($\nu_0 = c/(2L)$)
- the input power to the interferometer (P_{IN})
- the power recycling gain (g_{cr}^2)
- the arm cavity finesse ($\mathcal{F} = 220$)

- the input and output efficiency (ϵ)
- the laser wavelength ($\lambda = 1064 \times 10^{-9}$ m)

where we lump all losses due to absorption, scattering, or imperfect mode-matching, and the photodiode quantum efficiency, into the efficiency ϵ .

The predicted curve is produced by dividing the amplitude spectral density of the shot noise on the detection photodiode (A_{shot}) by the optical gain of the interferometer (S_{DC}). The optical gain is (as derived earlier) simply the derivative of the power at the output port with respect to changes in differential arm length, evaluated at the operating DARM offset.

$$A_{shot}(f) = \sqrt{2h(c/\lambda)P_{AS}} \quad (5.1)$$

$$S_{DC}(f) = 2\sqrt{\epsilon P_{IN} P_{AS}} g_{cr}^2 r_{cp} (1 + if/f_c)^{-1} \quad (5.2)$$

where $f_c = \nu_0/(2\mathcal{F})$ is the cavity pole, h is Planck's constant, and c is the speed of light. This expression for S_{DC} is in the single-pole approximation, which is valid for frequencies much lower than the arm cavities' free spectral range ($f \ll \nu_0$), and for frequencies above the test mass suspension's pendulum resonance (which may be increased due to radiation pressure).

Combining these two expressions gives the noise floor due to shot noise, calibrated in meters; dividing by L gives the noise floor in strain:

$$x_{shot}(f) = \sqrt{\frac{hc}{2\lambda\epsilon P_{IN}}} \frac{1}{g_{cr}^2 r_{cp}} \left| 1 + i\frac{f}{f_c} \right| \quad (5.3)$$

$$h_{shot}(f) = (1/L) x_{shot}(f) \quad (5.4)$$

The shot noise seen at the photodiode has a white spectrum; the entire shape of the shot noise when calibrated as a displacement or strain comes from the calibration (i.e. the optical gain) which in turn is shaped only by the cavity pole. Interferometers using signal recycling will have a more complicated response function.

5.1.1 Measured and expected sensitivity

The measured detector noise floors, calibrated as a displacement amplitude spectral density ($m/\sqrt{\text{Hz}}$), along with the expected performance based on equation 5.4 and measured detector parameters, are depicted in figure 5.1. The measured spectra were taken near the time of the detectors' highest inspiral ranges in summer 2010. The parameters used in the model are given in table 5.1.

The comparison reveals that the achieved performance is as expected. However, some comments are in order: The H1 detector was able to operate with about twice as much input power as the L1 detector, and had a power recycling gain approximately 40% better than L1's; from this we would expect considerably better shot noise level at H1. However, the H1 detector also experienced anomalously low transmission of the arm cavity mode through the

parameter	Hanford	Livingston
arm cavity phase gain	137	137
input optics efficiency	0.82	0.75
interferometer mode-matching		0.92
carrier recycling gain	59 ± 6	41
modulation depth	0.34	0.33
OMC transmission	0.97	
OMC mode-matching	0.70	0.95
Output Faraday transmission	0.94 ± 0.02	0.9805
DC-readout path pickoff	0.953	0.972
PD quantum efficiency	0.98	

Table 5.1: Designed and measured properties of the Hanford and Livingston interferometers.

output mode cleaner which contributed to a power efficiency (ϵ) much lower than desired. The poor OMC transmission was due to some combination of poor mode-matching, and high cavity losses which appeared near the end of the science run. These anomalous losses are not understood and are, as of the time of writing, under active investigation.

5.2 Laser and oscillator noise coupling mechanisms

For the purpose of computing the frequency response of the interferometer and the expected laser and oscillator noise couplings, it is convenient to regard the electric field at any given location in the interferometer as a comb of discrete spectral lines. Generically, we refer to any spectral line as a ‘sideband’. The sidebands are divided into radio-frequency (RF) sidebands and audio-frequency (AF) sidebands. The distinction is not actually the frequency of the lines but their magnitude; RF sidebands have some finite amplitude, while audio-frequency sidebands are infinitesimal. When the electric field is incident upon a photodiode, the photodiode will see a beat signal between every pair of sidebands. In our formalism we make the approximation that the product of any two audio-frequency sidebands is zero. Audio-frequency sidebands are used simply as test fields to evaluate linear transfer functions. They produce signals at PDs by beating against the finite-amplitude RF sidebands.

As detailed in the preceeding chapter, the state of the LIGO interferometer is determined by sampling the electric field at various ports using photodiodes. Pairs of RF sidebands at several distinct frequencies are introduced at the input to the interferometer; interference between these various fields allows the state of the interferometer to be determined. Around the laser carrier, there are two pairs of RF sidebands, each produced through phase modulation: the *resonant sideband* at ~ 25 MHz, which enters the interferometer and emerges at the output port; and the *non-resonant sideband* at ~ 61 MHz, which is mostly reflected by the power recycling mirror.

For an intuitive understanding of the noise couplings to DC readout, we will consider

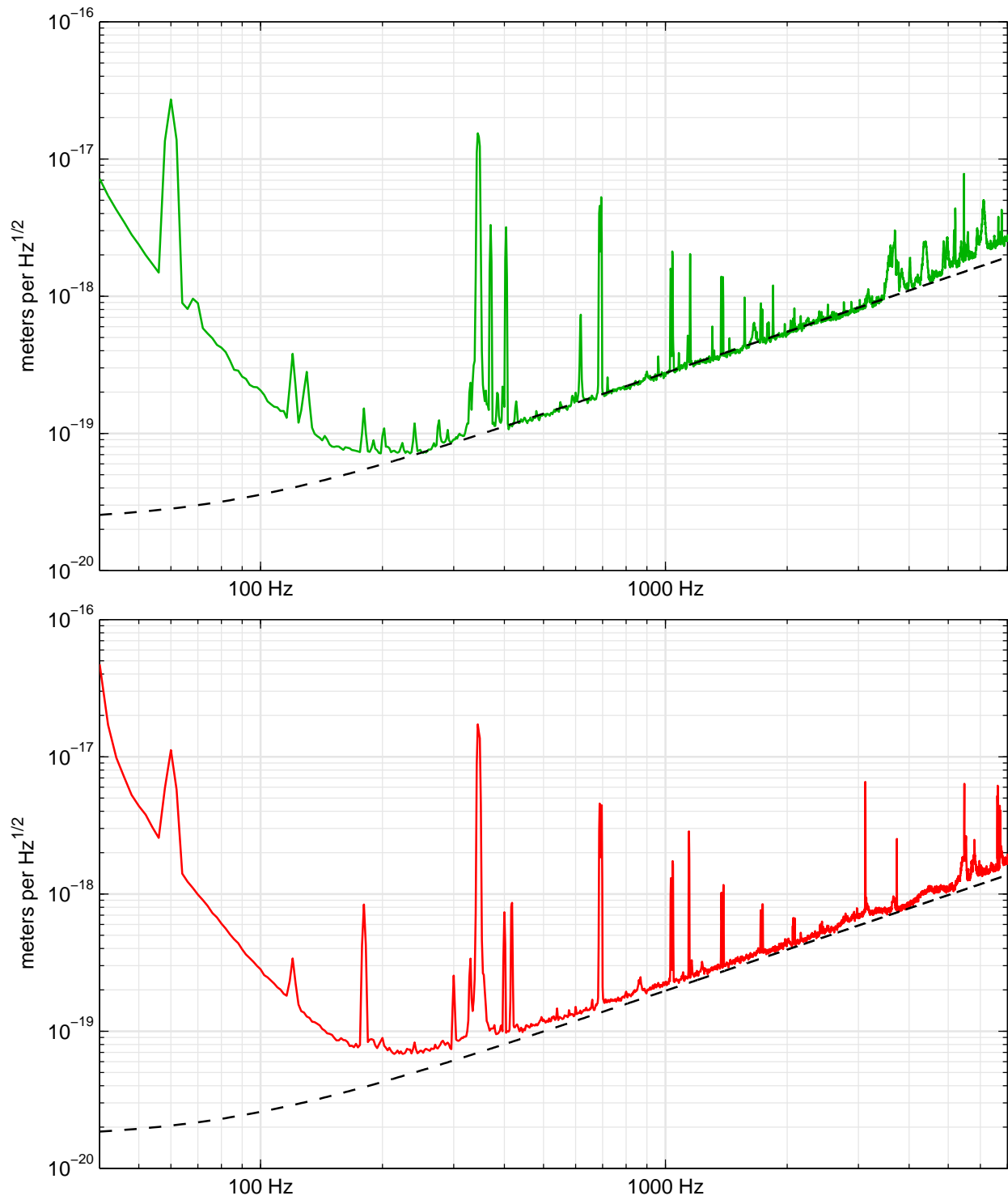


Figure 5.1: Shot noise limited sensitivity of the Livingston and Hanford detectors.

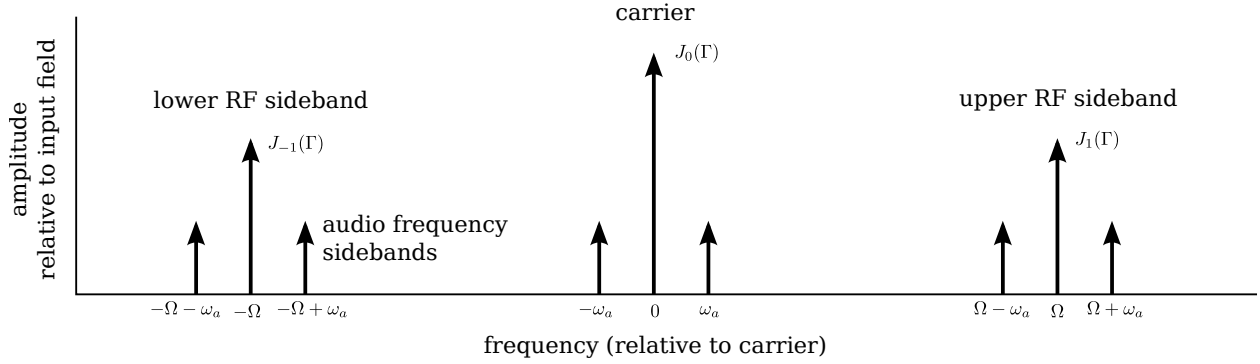


Figure 5.2: Schematic diagram of the laser carrier and RF sidebands, and their associated audio-frequency sidebands.

only the resonant sideband, and ignore the residual non-resonant sideband. In numerical simulations, both are included. The arrangement of RF sidebands is depicted in figure ??.

Sidebands are typically created in pairs around a modulated the parent field; and, when incident on a photodiode, they are most conveniently treated in pairs too. Instead of considering the amplitudes of upper and lower sidebands separately, we can instead use a basis where we quantify the sidebands as some amount of amplitude modulation (AM) and some amount of phase modulation.

5.2.1 Laser noises

The Michelson-based design of laser interferometer gravitational wave detectors is attractive due to its high common mode noise rejection. A Michelson interferometer with identical arms would completely isolate the output port from common-mode noises (i.e. noise introduced at the input port). Any asymmetries between the arms will introduce couplings of noises at the input port to the output port. Some such asymmetries are unintentional, such as the difference in finesse or reflectivity of the arms; intentional DARM and MICH asymmetries are introduced in order to allow the local oscillator (RF or carrier) to read the output port.

Laser intensity noise

Coupling of laser intensity noise to the output port is one of the easiest couplings to understand. The dominant mechanisms (in the absence of radiation pressure effects) are:

- Below the coupled-cavity pole ($f_{cc} \approx 1$ Hz), carrier power fluctuations are transmitted directly to the output port, attenuated only by the ratio P_{AS}/P_{IN} . Above the coupled cavity pole, transmission of AM on the carrier is attenuated by $1/f$.
- The resonant RF sidebands and any modulation they carry reaches the output port attenuated only slightly, since the Michelson is arranged (via the Schnupp asymmetry)

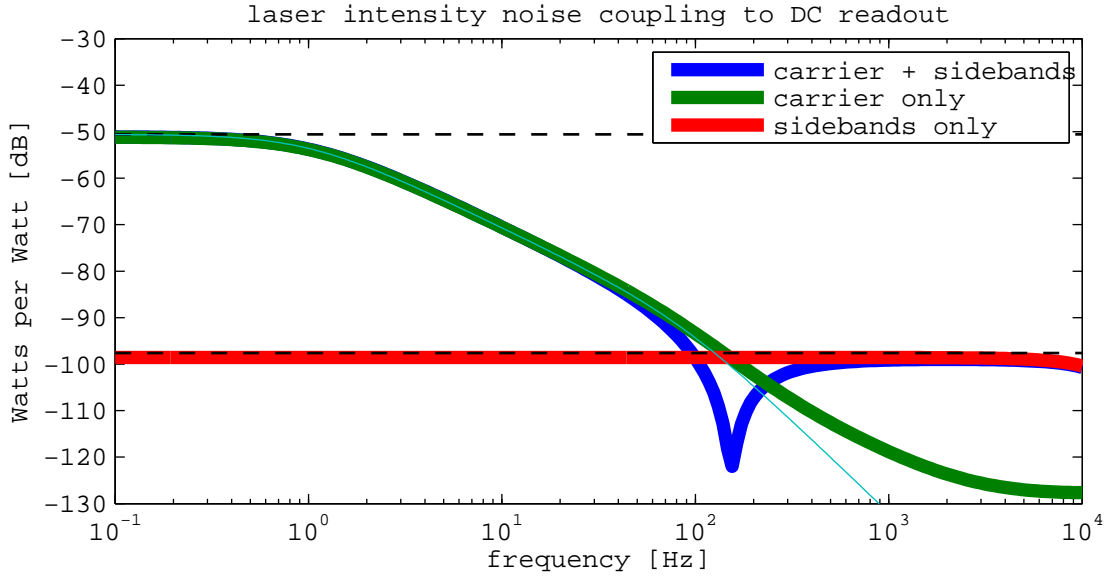


Figure 5.3: Direct contributions of amplitude modulation of the laser carrier and RF sidebands to DC readout, in the absence of radiation pressure. The carrier contribution is shaped by the coupled cavity pole. The RF contribution is due to residual off-resonance transmission through the OMC. Interference between the two coupling mechanisms creates a dip in the total coupling at the crossover frequency.

to conduct the RF sidebands to the output port. Because the RF sidebands are not resonant in the arms, noise on the RF sidebands is not attenuated by the coupled-cavity pole; instead they see a much lower finesse power recycling cavity and transmission is essentially flat in the band of interest. Once reaching the output port, however, the RF sidebands are strongly attenuated by the OMC.

At low frequency, the carrier contribution dominates; at higher frequency the residual RF sidebands dominate. This is depicted in figure 5.3.

Laser intensity noise creates a varying radiation pressure force in the arm cavities, which in turn causes displacement noise. To distinguish this effect from the inherent *quantum* radiation pressure noise[37], we refer to this as *technical* radiation pressure noise. For identical arm cavities, the effect would be entirely common mode. Differences in arm cavity finesse and (especially) the intentional differential detuning of the arm cavities produce a (potentially large[38]) coupling of technical radiation pressure noise to DARM.

Laser frequency noise

5.2.2 Oscillator noises

Reduced coupling of noises from the RF oscillator is one of the motivations for implementing DC readout. Despite not relying on the RF sidebands directly, behavior of the RF oscillator

is still able to enter into the DC readout signal through control loop cross-couplings, leakage of RF sideband power through the OMC, and amplitude modulation of the laser carrier induced via AM on the RF oscillator.

Oscillator AM

Amplitude fluctuations of the RF oscillator produce a fluctuating modulation depth; when the RF oscillator signal fluctuates upwards, more power is diverted from the carrier into the RF sidebands. The result is somewhat similar to laser AM, except that carrier AM and RF AM are anti-correlated instead of correlated.

Unlike laser AM, oscillator AM does not produce equal relative intensity noise (RIN) variations of the carrier and sidebands; this is simply because oscillator AM results in equal and opposite changes of power in the carrier and sideband rather than linear scalings of both. The sideband RIN per oscillator AM is given by

$$\frac{\text{SB RIN}}{\text{OSC AM}} = 2\Gamma_0 \frac{J'_1(\Gamma_0)}{J_1(\Gamma_0)} = \Gamma_0 \frac{J_0 - J_2}{J_1} \quad (5.5)$$

where Γ_0 is the nominal modulation depth, $J_n(z)$ is the n th Bessel function, and $J'_n(z) = (\partial/\partial z)J_n(z)$ is the derivative of the Bessel function.

Measured coupling is shown in figure ??.

Oscillator phase noise

Phase noise on the RF oscillator produces phase noise on the resulting RF sidebands, but does not affect the laser carrier. Its direct coupling to DC readout is therefore quite small; to couple to DC readout, the phase noise sidebands must be converted to AM through Michelson asymmetries, and then survive attenuation by the OMC.

5.3 Laser and oscillator noise coupling measurements

Laser and oscillator noise couplings were measured at both the H1 and L1 detectors¹, at a selection of DARM offsets. In this section I explain how the measurements were made and discuss the results.

5.3.1 Laser noise coupling measurements

The LIGO laser source contains an intensity stabilization servo (ISS) which reduces the relative intensity noise (RIN) of the laser power before the laser enters the interferometer. Injecting an excitation into the error point of this servo impresses intensity noise onto the

¹Measurements at Hanford were made by Nicolás Smith.

beam. The laser intensity noise coupling was measured by taking synchronous swept-sine transfer functions from a monitor photodiode just after the ISS and the DARM readout.

The laser frequency is stabilized to the mean length of the two arms (CARM) by a high-bandwidth analog servo, the common mode servo. Frequency modulation can be induced by injecting into the error point of this servo. Unlike with the ISS, there is no separate witness sensor to provide a direct measurement of the induced laser frequency modulation. Instead we must make a calibration of the common mode servo error point. The frequency noise coupling is to be calibrated in terms of Hz of frequency noise *before* the stabilizing action of the common mode servo, so we must account for the suppression of the loop. The calibration was done by porting the calibration of DARM to CARM, as follows:

1. Drive the position of one of the end test masses (ETMs) with a sinusoidal modulation at some probe frequency ($f = 7300$ Hz was used). In the absence of loops, this would produce equal DARM and CARM motion.
2. Measure the response in the DARM and CARM readouts. The CARM readout channel is REFL_I, which senses the mismatch between the laser carrier frequency and the CARM length.
3. Apply the DARM calibration. This includes compensation for the DARM control loop.
4. Compensate for the frequency noise suppression of the common mode loop by multiplying by $1 + G$ where G is the (complex) open loop gain of the common mode loop at the probe frequency.
5. Equate the calibrated DARM and loop-corrected CARM. This gives a calibration for CARM in meters at the probe frequency.
6. Multiply by $\delta\nu/\delta L = \nu/L = c/(\lambda L)$ to convert from meters to Hz.
7. Assume a model for the CARM to REFL_I transfer function to propagate the calibration to other frequencies. This transfer function is simply the coupled-cavity pole[23, eq. 3.5].

5.3.2 Oscillator noise coupling measurements

To measure oscillator noise couplings we temporarily switched the source of the 25 MHz oscillator from the Wenzel crystal oscillator to a general purpose (IFR 2023A) RF function generator, which accepts phase and amplitude modulation inputs. The measurements were made by connecting a spare DAC output to the modulation input of the IFR function generator and then taking synchronous swept-sine transfer functions from the modulation drive to the DC readout with the interferometer in its running configuration.

To calibrate the oscillator AM transfer function, we configured the interferometer optics (by misaligning unneeded mirrors) to send a fraction of the input light directly to the

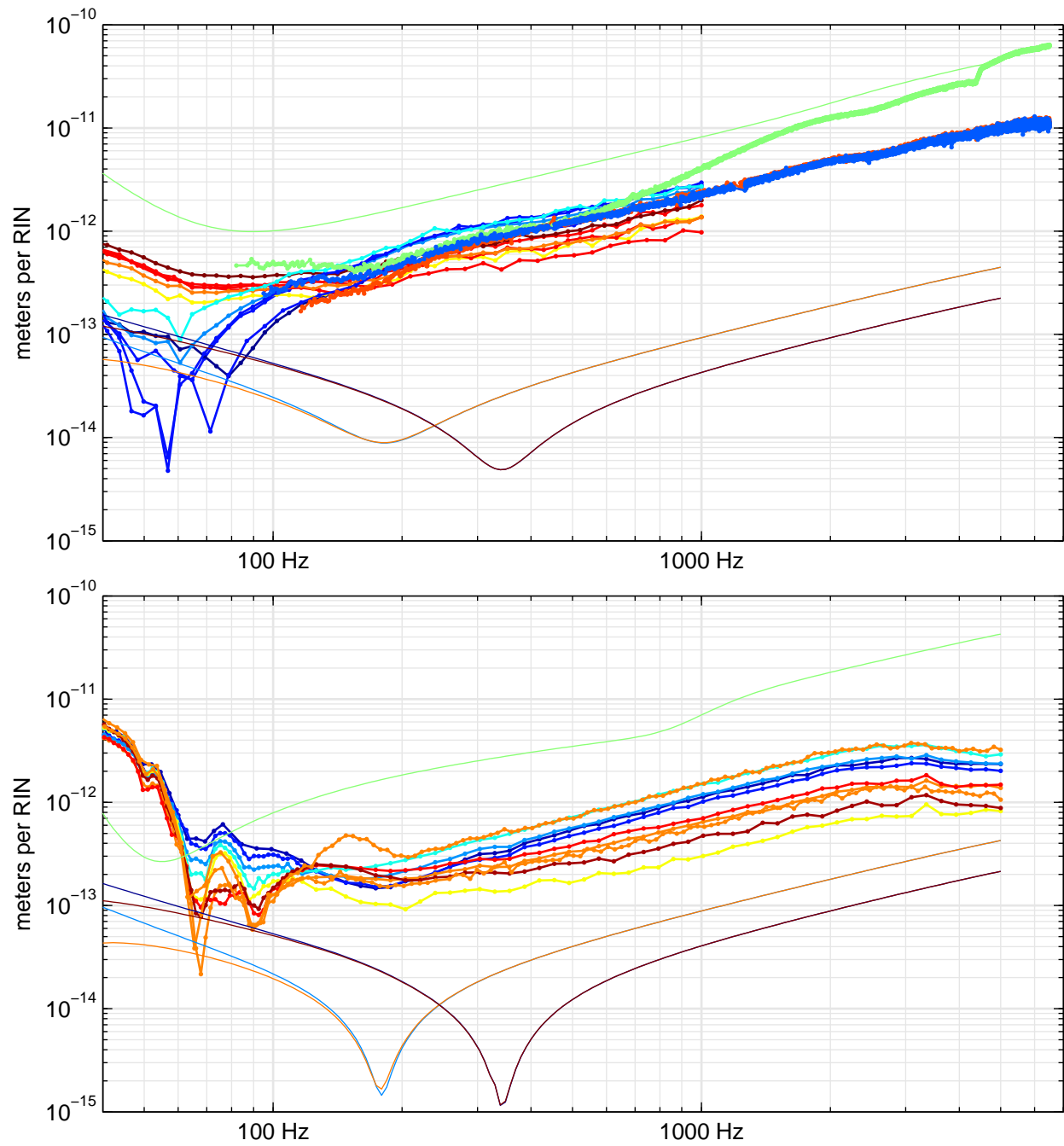


Figure 5.4: Laser intensity noise coupling to DARM. Solid lines are the results of a frequency-domain, plane-wave model; dotted lines are linear transfer function measurements. Color represents the DARM offset, with warm colors for positive offsets and cool colors for negative offsets. The upper plot is Livingston; the lower one is Hanford.

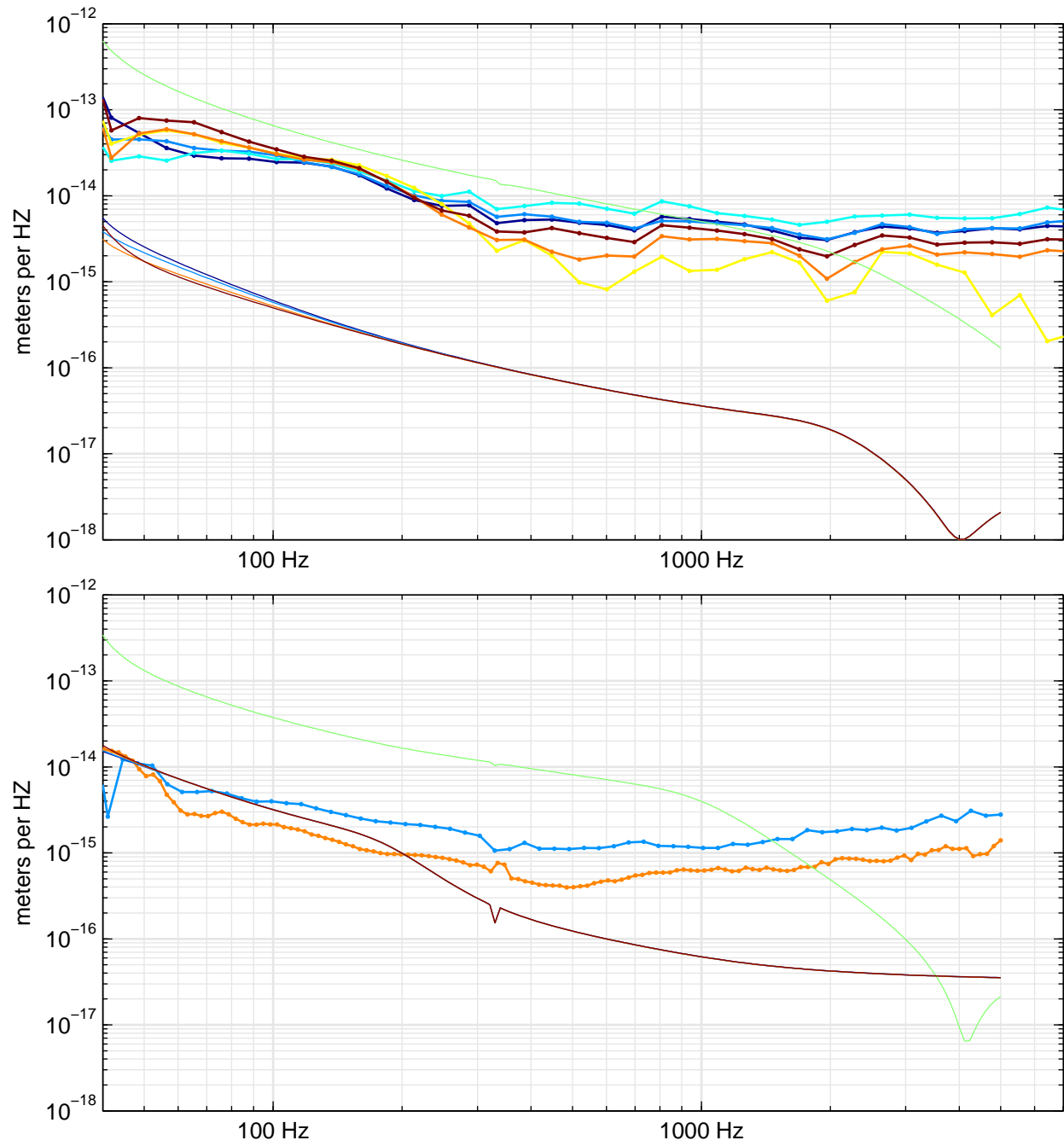


Figure 5.5: Laser frequency noise coupling to DARM

OMC and locked the OMC to one of the RF sidebands. Taking the transfer function in this configuration allowed a direct measurement of the AM imposed on the RF sidebands². To calibrate the oscillator PM transfer function, a curve with the same shape as the AM calibration was used, but with the DC value determined by the front panel setting of the phase modulation depth on the function generator. This was checked separately at a few individual frequencies by connecting the output of the function generator directly to an RF spectrum analyzer.

5.4 Beam jitter noise

Beam jitter noise is perhaps the most important new noise source in DC readout and is tied to alignment of the OMC, which has proved to be one of the most subtle new issues. The output mode cleaner converts motion of the input beam into variations in transmission. The resulting variation in the transmitted light level is indistinguishable from DARM motion.

5.5 Electronics noise

An optical power of 100 mW on the readout photodiodes will produce a photocurrent of $i = q_e \lambda / (hc) \cdot 100 \text{ mW} = 86 \text{ mA}$, which in turn has a shot noise floor of $\sqrt{2q_e i} \approx 500 \text{ pA}/\sqrt{\text{Hz}}$. Across $100 \text{ } \Omega$ transimpedance, this becomes $50 \text{ nV}/\sqrt{\text{Hz}}$. The noise floor of the readout electronics must be below this level and not be polluted by any baseband $1/f$ flicker noise.

The main strategy is to aggressively amplify the electronic signal as close to the photodiodes as possible, so that noises added downstream become insignificant. To eliminate even triboelectric effects, the first preamp stages are placed in-vacuum. The in-vacuum preamps consist of active filter stages with two zeros at 8 Hz and two poles at 80 Hz, for a factor of 100 amplification at 100 Hz. This is followed by two more pole-zero pairs in satellite amplifiers on the floor outside the vacuum chamber, for a total gain of 10,000 before the long run to the racks.

5.6 Optical spring

Detuning the arm cavities from their resonance introduces a big optical spring.

$$k_{opt} \approx \frac{64\mathcal{F}^2 g^2 P_{IN}}{c\lambda^2} (\delta x) \quad (5.6)$$

²Thank you to Robert Ward for suggesting the technique.

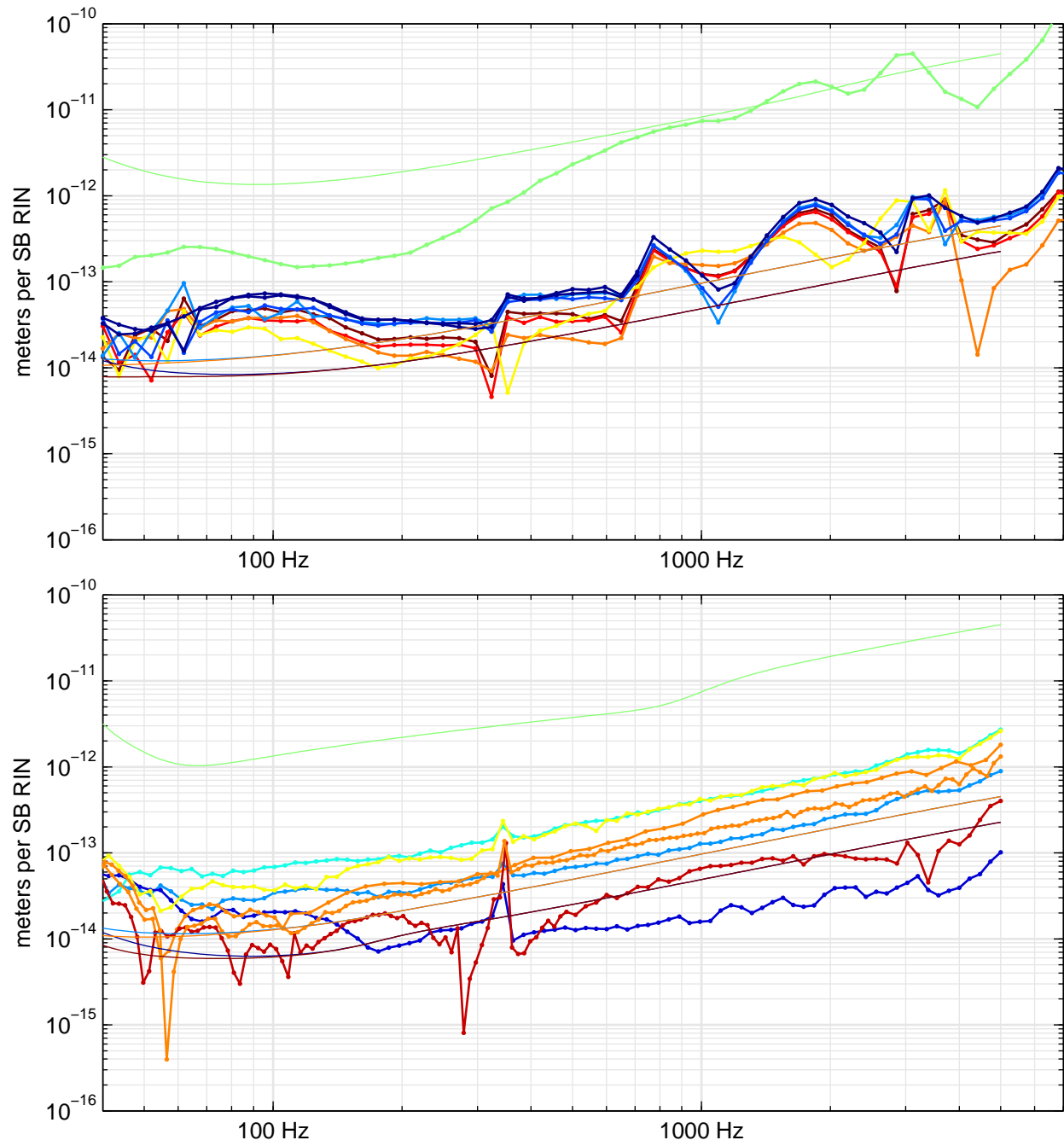


Figure 5.6: Oscillator amplitude noise coupling to DARM

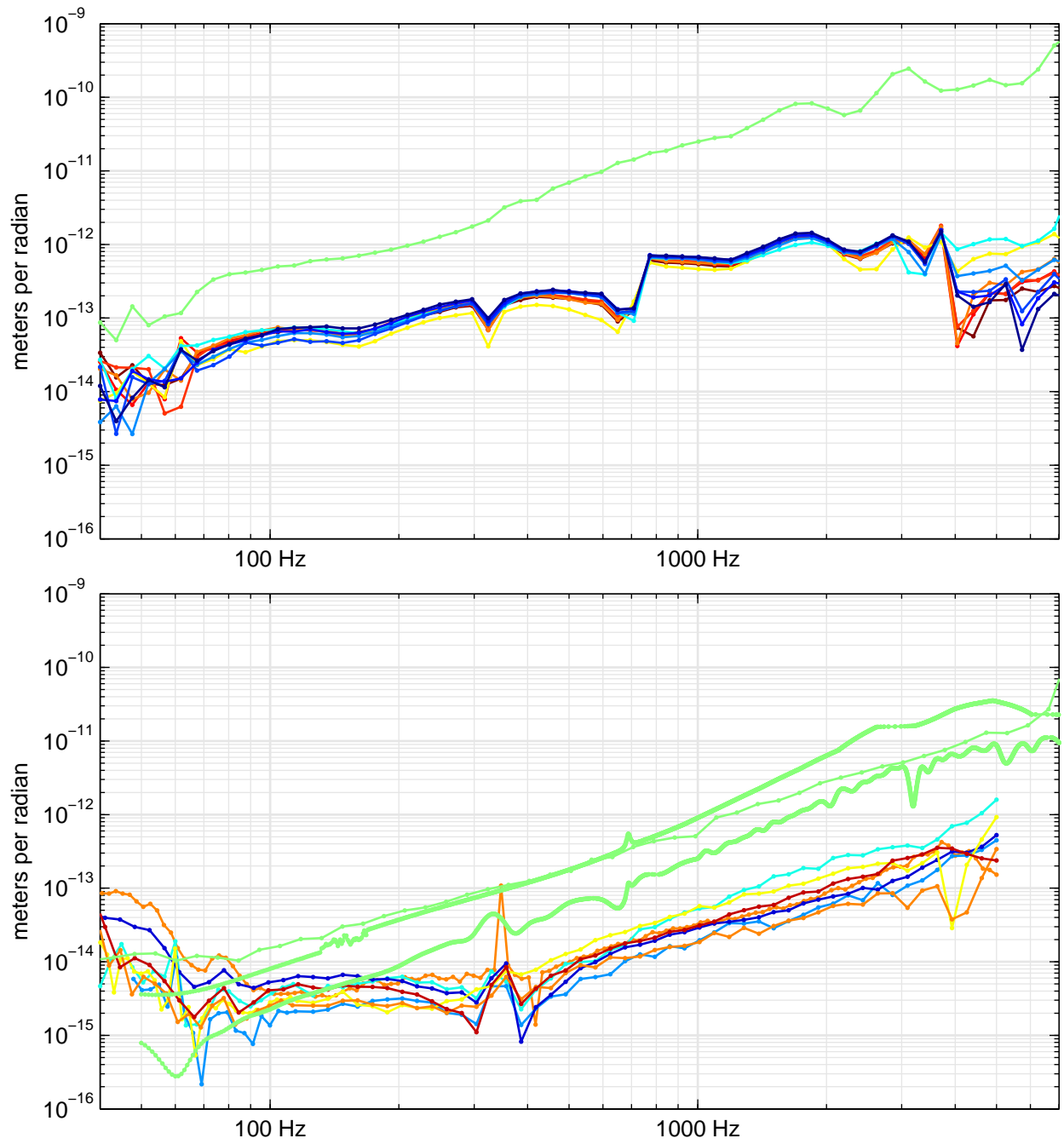


Figure 5.7: Oscillator phase noise coupling to DARM.

5.7 Technical radiation pressure noise

Amplitude noise on the input laser field produces modulation radiation pressure on the optics, in particular in the arm cavities. If the arm cavities were identical, this coupling would be entirely common mode. However, once the arms are differentially detuned, the radiation pressure noise attains a differential component.

We can treat the radiation pressure noise as a displacement noise.

Suppose the arm cavities are initially identical, with all suspensions having resonant frequency ω_0 . The optical spring shifts this resonance to $\omega_0 \pm \delta\omega$.

The intensity noise to displacement transfer function is

$$P_{IN} g_{rc}^2 g_{cav}^2 \frac{1}{s_{cc}} \quad (5.7)$$

5.8 Nonlinearity of the DC error signal

Although we operate sufficiently far from the dark fringe that the linear coupling of residual DARM motion to output power is dominant, sufficiently large motion could produce second-order coupling. Fortunately, this turns out to be totally negligible.

5.9 Digital effects

The realtime digital signal processing system through which our control systems are implemented provide the illusion of a continuous, analog system. However, it is important to remember that the underlying system operates on quantized values in discrete time in order to avoid being caught by surprise by “digital noises”.

- Finite, non-deterministic execution time
- ADC bit noise
- Floating point dynamic range
- Synchronized communications

5.10 Conclusion

6. Blargh

6.1 Abbreviations

AF	audio frequency
AM	amplitude modulation
AS	antisymmetric port
BS	beamsplitter
CARM	common arm length
DARM	differential arm length; the gravitational wave readout channel
DC	direct current (i.e. zero frequency)
ETM	end test mass
FSR	free spectral range
GW	gravitational wave
IFO	interferometer
ISS	intensity stabilization servo
ITMX	input test mass, X arm
LHO	LIGO Hanford Observatory
LIGO	Laser Interferometer Gravitational-wave Observatory
LLO	LIGO Livingston Observatory
MICH	Michelson interferometer
OMC	output mode cleaner
PD	photodiode
PM	phase modulation
PRC	power recycling cavity
RF	radio frequency
RIN	relative intensity noise ($\delta P/P$)
SNR	signal-to-noise ratio

6.2 symbols

ν_0	free spectral range
f	frequency (Hz)
f_c	cavity pole
\mathcal{F}	arm cavity finesse
s	Laplace parameter ($s = i\omega$)
ω	angular frequency ($\omega = 2\pi f$)
L	cavity length
ν	optical frequency (Hz)

Chapter 7

Appendix

7.1 Cavity stuff

A pole-zero map of the cavity amplitude reflectivity transfer function is shown in Fig. 7.1.

Using $\delta\nu/\nu = \delta L/L$ we can express the cavity pole as a length:

$$\delta L = \lambda (\delta\nu/\nu_0) = (1064nm)(85Hz/37kHz) \approx 2.4nm$$

$$\mathcal{F} = \frac{1}{2} \frac{\nu_0}{f_c} \quad (7.1)$$

where \mathcal{F} is the finesse, F is the coefficient of finesse, ν_0 is the free spectral range, f_c is the cavity pole, L is the cavity length.

7.2 The difference between PM and AM

Suppose we have a signal consisting of a carrier (at frequency ω and with unit amplitude) and two sidebands, of amplitudes a (lower) and b (upper), separated from the carrier by a frequency Ω :

$$E(t) = (1 + a \exp(-i\Omega t) + b \exp(i\Omega t)) \exp(i\omega t) \quad (7.2)$$

To find the power in this signal, we take the modulus squared, $P = E^*E$ where $*$ is the complex conjugate:

$$\begin{aligned} P = & (1 + |a|^2 + |b|^2) \\ & + (a^* + b) \exp(-i\Omega t) + (a + b^*) \exp(i\Omega t) \\ & + (ab^*) \exp(-2i\Omega t) + (a^*b) \exp(2i\Omega t) \end{aligned} \quad (7.3)$$

The condition for the 1Ω variation in the power to vanish is $a = -b^*$, i.e. the real parts of the amplitudes of the sidebands must be opposite, and the imaginary parts must be equal.

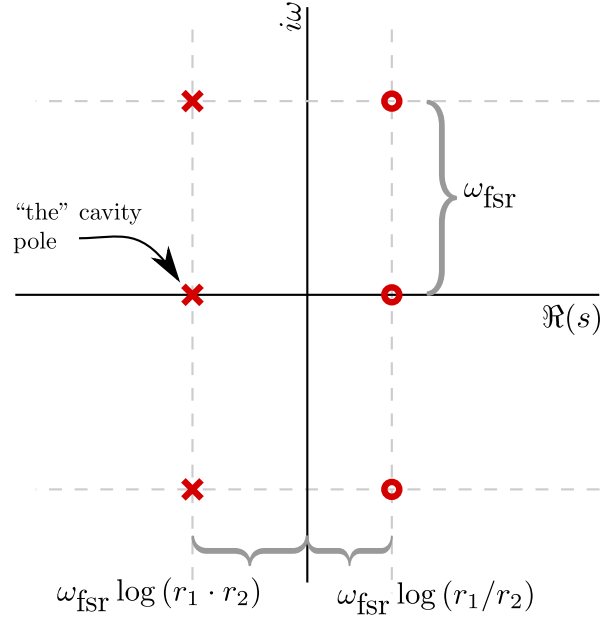


Figure 7.1: Pole-zero map of the cavity amplitude reflectivity. Poles are designated with \times and zeros with \circ ; r_1 is the amplitude reflectivity of the input coupler, and r_2 is the amplitude reflectivity of the output coupler. Losses can be lumped into r_2 . Notice that the free spectral range (angular frequency ω_{fsr}) sets the scale of the entire diagram, and the function is periodic in $i\omega$: there is an infinite line of poles and an infinite line of zeros. Two limiting cases are worth considering: (1) A critically-coupled cavity has $r_1 = r_2$, which brings the line of zeros onto the imaginary axis. On resonance, $i\omega$ travels through these zeros and the cavity reflectivity vanishes. This models the desired behavior of mode cleaner cavities. (2) A maximally over-coupled cavity has $r_2 = 1$, in which case the line of poles and line of zeros are equally spaced from the imaginary axis. This models the LIGO arm cavities. The cavity's amplitude transmission has the same poles as the reflectivity but no zeros.

So we can extract the amplitude and phase modulation indices:

$$\begin{aligned} m_{AM} &= (a + b^*) \\ m_{PM} &= (a - b^*) \end{aligned} \quad (7.4)$$

What is the condition for the 2Ω signal to vanish? With just two sidebands, it will always be present (though at second order in the sideband amplitude). In true phase modulation, the 2Ω signal is cancelled by the interaction of (the infinite number of) higher-order sidebands. As best I can tell, there is no simple arrangement of this cancellation other than via a magical property of the Bessel functions.

7.3 The difference between PM and FM

There is not really any difference between phase modulation and frequency modulation. Frequency modulation with modulation depth m_{FM} [Hz] at a frequency f [Hz] has the form

$$y(t) = \exp\{i\omega t\} \exp\left\{i \int_0^t 2\pi m_{\text{FM}} \Re\left\{e^{i2\pi ft'}\right\} dt'\right\} \quad (7.5)$$

where ω [radians/second] is the carrier frequency. We can simply do the integral and get:

$$y(t) = \exp\{i\omega t\} \exp\left\{i \frac{1}{f} m_{\text{FM}} \Re\left\{ie^{i2\pi ft}\right\}\right\} \quad (7.6)$$

which is just phase modulation at frequency f [Hz] with modulation depth $(i/f)m_{\text{FM}}$ (in radians). The relation between phase modulation and frequency modulation is therefore:

$$m_{\text{PM}} = \left(\frac{i}{f}\right) m_{\text{FM}}$$

The i signifies a phase shift of 90 degrees in the modulation (turning cos to sin).

7.4 Only the signal field matters

Suppose we have two electric fields incident on a photodiode: the signal field A_s and the local oscillator field A_{LO} . The power seen by the photodiode is

$$|A_s + A_{LO}|^2 = |A_s|^2 + |A_{LO}|^2 + 2\text{Re}A_s^* A_{LO}$$

In the small-signal regime, $|A_s| \ll |A_{LO}|$. The signal on the photodiode is proportional to $A_s A_{LO}$ while the shot noise is proportional to $\sqrt{|A_s|^2 + |A_{LO}|^2} \approx A_{LO}$. The detected SNR is independent of the local oscillator strength.

7.5 Optical phase conventions

7.6 The optical spring

When detuned from resonance, the power circulating within a Fabry-Perot cavity varies linearly with small deviations from that detuning. This gives rise to a displacement-dependent force, which can be described via a spring constant. This effect is called the *optical spring*¹.

For frequencies that are slow compared to the cavity pole, we can calculate the behavior of the spring using a quasi-static approximation, simply using the derivative of the power buildup versus cavity detuning.

The power circulating in a cavity is:

$$\frac{P_+}{P_{IN}} = \frac{g^2}{1 + F \sin^2 \phi} \quad (7.7)$$

where P_{IN} is the incident power, P_+ is the forward-circulating power, $g^2 = (t_1)^2 / (1 - r_1 r_2)$ is the power buildup on resonance, $F = 4r_1 r_2 / (1 - r_1 r_2)^2$ is the coefficient of finesse², and ϕ is the one-way phase detuning of the cavity, which is related to cavity length x as $\phi = (2\pi/\lambda)x$.

For a given power circulating in the cavity, the radiation pressure force due to the intra-cavity power on each of the mirrors is $f = 2P/c$. We can find the spring constant by taking the derivative:

$$k \equiv -\frac{\partial f}{\partial x} = -\frac{\partial}{\partial x} \frac{2P}{c} = -\frac{2}{c} \frac{\partial \phi}{\partial x} \frac{\partial P}{\partial \phi}$$

Working out the derivative, we find:

$$\frac{\partial}{\partial \phi} P_+ = -2Fg^2 \frac{\cos(\phi) \sin(\phi)}{(1 + F \sin^2 \phi)^2} P_{IN} \quad (7.8)$$

$$= -2Fg^2 P_{IN} \phi + O(\phi^3) \quad (7.9)$$

Putting it all together, we get:

$$k = 2Fg^2 \left(\frac{2P_{IN}}{c} \right) \left(\frac{2\pi}{\lambda} \right) \frac{\cos(\phi) \sin(\phi)}{(1 + F \sin^2 \phi)^2} \quad (7.10)$$

$$\approx 2Fg^2 \left(\frac{2P_{IN}}{c} \right) \left(\frac{2\pi}{\lambda} \right) \frac{\phi}{(1 + F \phi^2)^2} \quad (7.11)$$

$$\approx 2Fg^2 \left(\frac{2P_{IN}}{c} \right) \left(\frac{2\pi}{\lambda} \right) \phi + O(\phi^3) \quad (7.12)$$

¹This is the longitudinal optical spring; the angular optical spring arises due to other effects.

²The finesse (\mathcal{F}) is related to the coefficient of finesse (F) via $\mathcal{F} \approx \frac{\pi}{2} \sqrt{F}$.

where, of course, $\phi = (2\pi/\lambda)\delta x$, where x is the (one-way) detuning length. If a mirror is displaced by (δx) , the spring constant is:

$$k \approx \frac{64\mathcal{F}^2 g^2 P_{IN}}{c\lambda^2} (\delta x)$$

Putting in some numbers for the Enhanced LIGO arms:

$$\begin{array}{r} \mathcal{F} = 220 \\ g^2 = 137 \\ P_{IN} = 400 \text{ Watts} \\ \lambda = 1064 \text{ nm} \\ \delta x = 5 \text{ pm} \\ \hline k \approx 2500 \text{ N/m} \end{array}$$

For comparison, the mechanical restoring force has a spring constant of approximately

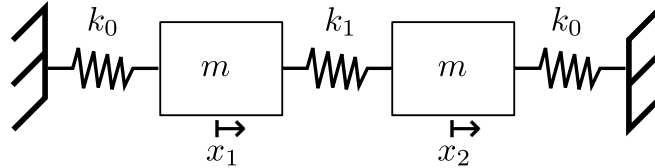
$$k_m = m\omega^2 \approx (10.5 \text{ kg}) (2\pi \cdot 0.75 \text{ Hz})^2 \approx 230 \frac{\text{N}}{\text{m}}$$

It can also be handy to put Eq. 7.11 into terms of the unitless detuning parameter $\delta_\gamma = \sqrt{F}\phi$, where $\delta_\gamma \equiv \frac{\delta}{\gamma}$, where δ is the cavity detuning (in radians/sec), and γ is the line-width (cavity pole) in the same units. If we further assume that the cavity is strongly-overcoupled, we can use the relations $g^2 = \sqrt{F} = \frac{2}{\pi}\mathcal{F} = 4/T_1$. With these substitutions (and $\lambda = 2\pi c/w_0$), we recover expression (3.14) given in Thomas Corbitt's thesis [39]:

$$K_0 \approx \frac{64P_{IN}w_0}{T^2c^2} \frac{\delta_\gamma}{(1 + \delta_\gamma^2)^2} \quad (7.13)$$

7.6.1 Coupled oscillators

Consider a system of two masses, connected to each other via a spring with spring constant k_1 and each connected to the wall via a spring of spring constant k_0 . (Later, k_0 will represent the pendula by which the optics are suspended, and k_1 will represent the optical spring.)



By inspection, the equations of motion are:

$$m\ddot{x}_1 = -k_0x_1 + k_1(x_2 - x_1) \quad (7.14)$$

$$m\ddot{x}_2 = -k_0x_2 - k_1(x_2 - x_1) \quad (7.15)$$

which may be written in matrix form as

$$\ddot{\mathbf{x}} = \frac{1}{m} \begin{bmatrix} -(k_0 + k_1) & k_1 \\ k_1 & -(k_0 + k_1) \end{bmatrix} \mathbf{x} \quad (7.16)$$

Because of the form of the matrix³, we can immediately see that it has eigenvectors corresponding to common and differential motion, with eigenvalues $\{-k_0, -(k_0 + 2k_1)\}$.

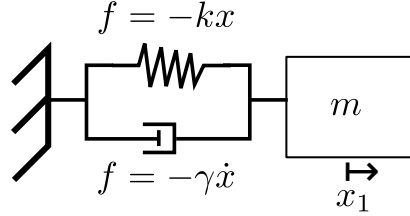
Applying this diagonalization, we find:

$$\ddot{\mathbf{x}}' = \frac{1}{m} \begin{bmatrix} -k_0 & 0 \\ 0 & -(k_0 + 2k_1) \end{bmatrix} \mathbf{x}' \text{ where } \mathbf{x}' = \begin{bmatrix} 1 & 1 \\ 1 & -1 \end{bmatrix} \mathbf{x}$$

The presence of the coupling k_1 only affects the differential mode.

7.6.2 Damped oscillators

Now consider a mass connected to the wall via a spring with spring constant k and a velocity damper with damping constant γ :



The equation of motion of the mass is:

$$m\ddot{x} = -kx - \gamma\dot{x} + f_{external} \quad (7.17)$$

with Laplace transform

$$ms^2X = -kX - \gamma sX + F_{external} \quad (7.18)$$

giving rise to a transfer function of

$$\begin{aligned} \frac{X}{F} &= \frac{1}{ms^2 + \gamma s + k} \\ &= \left(\frac{1}{m}\right) \frac{1}{(s - s_+)(s - s_-)} \text{ with } s_{\pm} = -\frac{1}{2}\frac{\gamma}{m} \pm \frac{1}{2}\sqrt{\left(\frac{\gamma}{m}\right)^2 - 4\frac{k}{m}} \end{aligned}$$

³The matrix $\begin{bmatrix} a & b \\ b & a \end{bmatrix}$ has eigenvectors $\begin{pmatrix} 1 \\ 1 \end{pmatrix}$ and $\begin{pmatrix} 1 \\ -1 \end{pmatrix}$ with eigenvalues $(a + b)$ and $(a - b)$.

7.6.3 Optickle

In the attached Matlab code, I construct a very simple model in Optickle[40] consisting of only a laser and two mirrors, forming a resonant cavity. Optickle is also supplied with the mechanical (force to position) transfer functions of each optic (in isolation). Together these transfer functions compose the *reaction matrix*, which is diagonal in the sense that force applied to one optic only affects the position of that same optic.

After constructing the model, we call Optickle via the tickle function:

```
[fDC, sigDC, sigAC, mMech, noiseAC, noiseMech] = tickle(opt, pos, f);
```

The output we are interested in here is “mMech,” which gives the modifications to the mechanical transfer functions due to the radiation pressure couplings. Its units are “meters per meter”—a bit perplexing at first but some intuition may be gained by considering it as (meters in the presense of radiation pressure)/(meters in the absense of radiation pressure). A more sensible approach is to multiply mMech with the reaction matrix, which gives the mechanical transfer functions (from force applied at some optic to displacement of every other optic) including all optomechanical couplings.

To extract the optical spring transfer function, I further transform mMech to the basis of common and differential degrees of freedom.

Because we know the mass, resonant frequency, and damping coefficient (and thus also the equivalent spring constant) of the mechanical transfer functions supplied to Optickle, we can compute the expected differential mode transfer function in the presence of radiation pressure by adjusting the spring constant from k to $k + 2k_{opt}$ where k_{opt} is the calculated optical spring constant, or simply shifting the resonance to $w' = w - \sqrt{2k_{opt}/m}$.

This approach shows good agreement (see Figure 7.2) with the results returned by Optickle with the caveat that **I’ve omitted that factor of two** and am instead using $k' = k + k_{opt}$. I currently believe this is an error in Optickle.

7.7 Gaussian beams

The general picture of Gaussian beams is shown here:

It is convenient to introduce teh complex beam parameter q . In terms of q :

$$\frac{1}{q(z)} = \frac{1}{R(z)} - i \frac{\lambda}{\pi w^2(z)} \quad (7.19)$$

where $R(z)$ is the radius of curvature of the phase fronts at a position z along the optical axis, and $w(z)$ is the spot size at that location. We can also write: $q(z) = iz_R + (z - z_0)$.

For a mode to resonate in an optical cavity, the spherical surface of the mirrors must match the spherical phase front of the beam at the location of the mirror.

Suppose mirror 1 has curvature R_1 and coordinate z_1 , and similarly for mirror 2. We would like to solve for the waist location and Rayleigh range.

References: Kogelnik and Li [41], Siegman [42].

7.8 Laser modes

The eigenmodes of an optical cavity formed from spherical lenses are the Hermite-Gauss (if the cavity has rectangular symmetry) or Laguerre-Gauss (for axial symmetry) modes. The amplitude distribution at the beam waist is a Gaussian multiplied by a Hermite or Laguerre polynomial. These are exactly the same families of functions as the energy eigenstate wavefunctions of the simple harmonic oscillator in quantum mechanics.

7.9 Control theory basics

Operation of the LIGO detectors relies crucially on feedback control systems. In general, the response of the optical plant is very nonlinear; in order to produce a valid readout, the plant must be held very close to its operating point. The use of feedback control allows us to attain linear response from an otherwise very nonlinear machine.

Here is a basic diagram of a feedback system:

Algebraically, one can derive a relationship giving the transfer function of the closed-loop system in the Laplace domain:

7.10 The Antenna Pattern

Gravitational waves come in two polarizations; for waves impinging from a given direction, the second polarization represents an ellipse of oscillating transverse strains rotated 45 degrees relative to the first.

Fundamentally, a Michelson interferometer is sensitive to two polarizations of gravitational waves. However, as seen in FIXME, we elect to throw away sensitivity to one polarization in return for common-mode noise immunity in the second polarization.

Although the waves come in two polarizations, one should note that there is no globally consistent notion of *the* h_+ and h_\times polarizations. This is forbidden by the Hairy Ball theorem.

For a single detector, we can identify h_+ as the polarization that shows up in DARM, and h_\times as the polarization that would show up in CARM. Immediately (again due to the hairy ball theorem) we see that there must be nulls in the sensitivity pattern of a single interferometer.

7.11 Shot Noise

The root-mean-square of a Poisson process with current I and quantum q measured over a bandwidth of Δf is

$$\sigma = \sqrt{2qI\Delta f}$$

Here I could be the electric current in Amps (=Coulombs/second) and q the charge of an electron. For light incident on a photodiode, the photon shot noise can be considered as an energy current, with $I \leftarrow P$ being the DC power, and $q \leftarrow h\nu$ being the energy per photon.

The amplitude spectral density of this process is white, with amplitude $\sqrt{2qI}$ in units of [I] per square root of Hz.

So, for power P , the shot noise amplitude spectral density is

$$\text{shot noise ASD} = \sqrt{2h\nu P} \quad [\text{Watts}/\sqrt{\text{Hz}}] \quad (7.20)$$

for a relative intensity noise of $\sqrt{2h\nu/P}$.

7.12 Noise analysis of opamp circuits

7.13 References

[43]

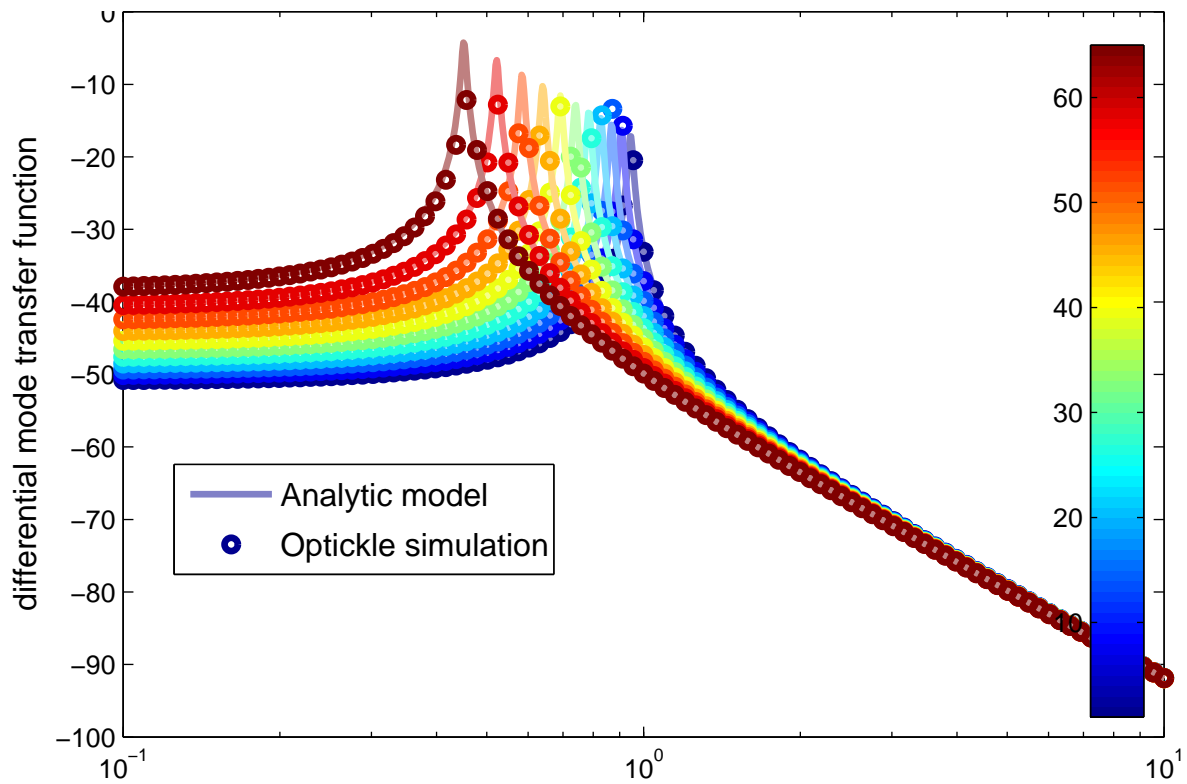


Figure 7.2: Comparison of a numerical (Optickle) model with analytically-derived results. The units of the y-axis are $20 \log_{10}(\text{displacement/force})$; the x-axis is Hz; color indicates cavity detuning in picometers.

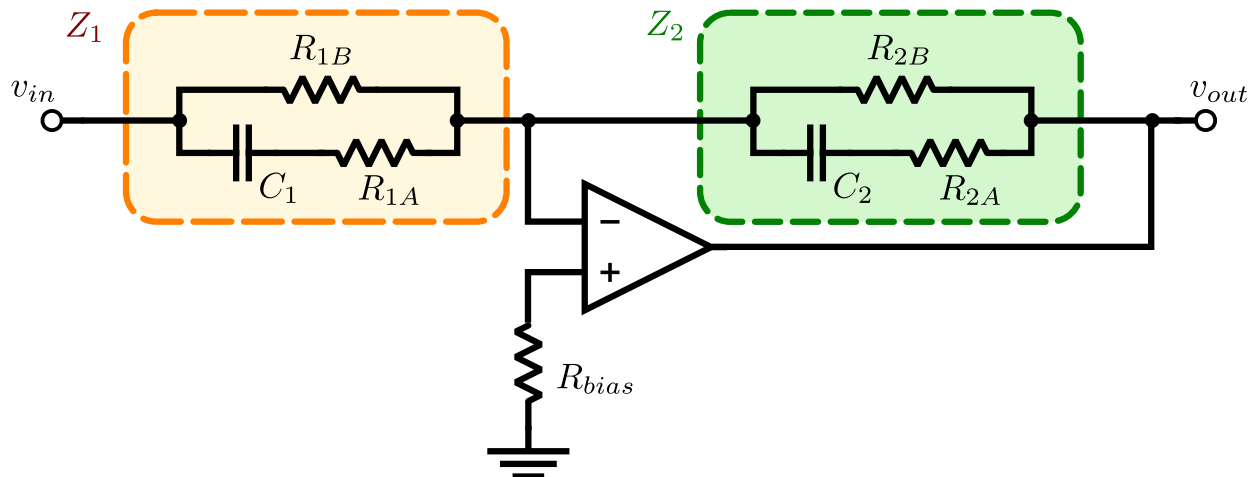


Figure 7.3: Basic active filter in the inverting amplifier configuration.

Bibliography

- [1] Bernard F. Schutz. Gravitational waves on the back of an envelope. *American Journal of Physics*, 52(5):412–419, 1984. URL: <http://dx.doi.org/10.1119/1.13627>, doi: 10.1119/1.13627.
- [2] Sean M. Carroll. Lecture Notes on General Relativity. December 1997. URL: <http://preposterousuniverse.com/grnotes/>, arXiv:gr-qc/9712019.
- [3] R. A. Hulse and J. H. Taylor. Discovery of a pulsar in a binary system. *Astrophys. J. Lett.*, 195:L51–L53, January 1975. URL: <http://dx.doi.org/10.1086/181708>, doi: 10.1086/181708.
- [4] J. M. Weisberg and J. H. Taylor. The Relativistic Binary Pulsar B1913+16: Thirty Years of Observations and Analysis. In F. A. Rasio & I. H. Stairs, editor, *Binary Radio Pulsars*, volume 328 of *Astronomical Society of the Pacific Conference Series*, July 2005. URL: <http://arxiv.org/abs/astro-ph/0407149>, arXiv:astro-ph/0407149.
- [5] A. G. Lyne, M. Burgay, M. Kramer, A. Possenti, R. N. Manchester, F. Camilo, M. A. McLaughlin, D. R. Lorimer, N. D’Amico, B. C. Joshi, J. Reynolds, and P. C. C. Freire. A Double-Pulsar System: A Rare Laboratory for Relativistic Gravity and Plasma Physics. *Science*, 303(5661):1153–1157, February 2004. URL: <http://arxiv.org/abs/astro-ph/0401086>, doi:10.1126/science.1094645.
- [6] M. Kramer, I. H. Stairs, R. N. Manchester, M. A. McLaughlin, A. G. Lyne, R. D. Ferdman, M. Burgay, D. R. Lorimer, A. Possenti, N. D’Amico, J. M. Sarkissian, G. B. Hobbs, J. E. Reynolds, P. C. C. Freire, and F. Camilo. Tests of General Relativity from Timing the Double Pulsar. *Science*, 314(5796):97–102, October 2006. URL: <http://dx.doi.org/10.1126/science.1132305>, doi:10.1126/science.1132305.
- [7] B. Knispel, B. Allen, J. M. Cordes, J. S. Deneva, D. Anderson, C. Aulbert, N. D. R. Bhat, O. Bock, S. Bogdanov, A. Brazier, F. Camilo, D. J. Champion, S. Chatterjee, F. Crawford, P. B. Demorest, H. Fehrmann, P. C. C. Freire, M. E. Gonzalez, D. Hammer, J. W. T. Hessels, F. A. Jenet, L. Kasian, V. M. Kaspi, M. Kramer, P. Lazarus, J. van Leeuwen, D. R. Lorimer, A. G. Lyne, B. Machenschalk, M. A. McLaughlin, C. Messenger, D. J. Nice, M. A. Papa, H. J. Pletsch, R. Prix, S. M. Ransom, X. Siemens, I. H. Stairs, B. W. Stappers, K. Stovall, and A. Venkataraman. Pulsar Discovery by Global Volunteer Computing. *Science*, 329(5997):1305, September 2010. URL: <http://dx.doi.org/10.1126/science.1195253>, doi:10.1126/science.1195253.

- [8] Rainer Weiss. Electromagnetically Coupled Broadband Gravitational Antenna. *Quarterly Progress Reports of the Research Laboratory for Electronics*, 105:54–76, April 1972. URL: <http://www.ligo.caltech.edu/docs/P/P720002-01/P720002-01.pdf>.
- [9] Robert L. Forward. Wideband laser-interferometer gravitational-radiation experiment. *Physical Review D*, 17(2):379–390, January 1978. URL: <http://dx.doi.org/10.1103/PhysRevD.17.379>, doi:10.1103/PhysRevD.17.379.
- [10] G. Hobbs, A. Archibald, Z. Arzoumanian, D. Backer, M. Bailes, N. D. R. Bhat, M. Burgay, S. Burke-Spolaor, D. Champion, I. Cognard, W. Coles, J. Cordes, P. Demorest, G. Desvignes, R. D. Ferdman, L. Finn, P. Freire, M. Gonzalez, J. Hessels, A. Hotan, G. Janssen, F. Jenet, A. Jessner, C. Jordan, V. Kaspi, M. Kramer, V. Kondratiev, J. Lazio, K. Lazaridis, K. J. Lee, Y. Levin, A. Lommen, D. Lorimer, R. Lynch, A. Lyne, R. Manchester, M. McLaughlin, D. Nice, S. Osłowski, M. Pilia, A. Possenti, M. Purver, S. Ransom, J. Reynolds, S. Sanidas, J. Sarkissian, A. Sesana, R. Shannon, X. Siemens, I. Stairs, B. Stappers, D. Stinebring, G. Theureau, R. van Haasteren, W. van Straten, J. P. W. Verbiest, D. R. B. Yardley, and X. P. You. The international pulsar timing array project: using pulsars as a gravitational wave detector. *Classical and Quantum Gravity*, 27, November 2009. URL: <http://arxiv.org/abs/0911.5206>, arXiv:0911.5206.
- [11] Rana Adhikari, Peter Fritschel, and Sam Waldman. Enhanced LIGO. Technical Report T060156-01-I, LIGO Laboratory, July 2006. URL: <http://www.ligo.caltech.edu/docs/T/T060156-01.pdf>.
- [12] Peter Fritschel, Rana Adhikari, and Rai Weiss. Enhancements to the LIGO S5 Detectors. Technical Report T050252-00-I, LIGO Laboratory, November 2005. URL: <http://www.ligo.caltech.edu/docs/T/T050252-00.pdf>.
- [13] J. R. Smith and for the LIGO Scientific Collaboration. The path to the enhanced and advanced LIGO gravitational-wave detectors. *Classical and Quantum Gravity*, 26(11):114013+, June 2009. URL: <http://dx.doi.org/10.1088/0264-9381/26/11/114013>, doi:10.1088/0264-9381/26/11/114013.
- [14] Volker Quetschke. Electro-Optic Modulators and Modulation for Enhanced LIGO and Beyond. In *Coherent Optical Technologies and Applications*, pages CMC1+. Optical Society of America, July 2008. URL: <http://www.opticsinfobase.org/abstract.cfm?id=169025>.
- [15] R. L. Ward, R. Adhikari, B. Abbott, R. Abbott, D. Barron, R. Bork, T. Fricke, V. Frolov, J. Heefner, A. Ivanov, O. Miyakawa, K. McKenzie, B. Slagmolen, M. Smith, R. Taylor, S. Vass, S. Waldman, and A. Weinstein. DC readout experiment at the Caltech 40m prototype interferometer. *Classical and Quantum Gravity*, 25(11):114030+, 2008. URL: <http://dx.doi.org/10.1088/0264-9381/25/11/114030>, doi:10.1088/0264-9381/25/11/114030.

- [16] Robert L. Ward. *Length Sensing and Control of an Advanced Prototype Interferometric Gravitational Wave Detector*. PhD thesis, California Institute of Technology, Pasadena, CA, February 2010. URL: <http://thesis.library.caltech.edu/5836/>.
- [17] S. Hild, H. Grote, J. Degallaix, S. Chelkowski, K. Danzmann, A. Freise, M. Hewitson, J. Hough, H. Luck, M. Prijatelj, K. A. Strain, J. R. Smith, and B. Willke. DC-readout of a signal-recycled gravitational wave detector. *Classical and Quantum Gravity*, 26(5):055012+, March 2009. URL: <http://dx.doi.org/10.1088/0264-9381/26/5/055012>, doi:10.1088/0264-9381/26/5/055012.
- [18] M. Prijatelj, H. Grote, J. Degallaix, M. Hewitson, S. Hild, C. Affeldt, A. Freise, J. Leong, H. Lück, K. A. Strain, H. Wittel, B. Willke, and K. Danzmann. Control and automatic alignment of the output mode cleaner of GEO 600. *Journal of Physics: Conference Series*, 228(1):012014+, May 2010. URL: <http://dx.doi.org/10.1088/1742-6596/228/1/012014>, doi:10.1088/1742-6596/228/1/012014.
- [19] J. Degallaix, H. Grote, M. Prijatelj, M. Hewitson, S. Hild, C. Affeldt, A. Freise, J. Leong, H. Lück, K. A. Strain, H. Wittel, B. Willke, and K. Danzmann. Commissioning of the tuned DC readout at GEO 600. *Journal of Physics: Conference Series*, 228(1):012013+, May 2010. URL: <http://dx.doi.org/10.1088/1742-6596/228/1/012013>, doi:10.1088/1742-6596/228/1/012013.
- [20] F. Acernese and et al. The Virgo 3 km interferometer for gravitational wave detection. *Journal of Optics A: Pure and Applied Optics*, 10(6):064009+, June 2008. URL: <http://dx.doi.org/10.1088/1464-4258/10/6/064009>, doi:10.1088/1464-4258/10/6/064009.
- [21] M. Abernathy and Others. Einstein Telescope Design Study. Technical report, Einstein Telescope Science Team, May 2011. URL: <https://tds.ego-gw.it/itf/tds/index.php?callContent=2&callCode=8192&srchCode=0106A>.
- [22] B. P. Abbott and et al. LIGO: the Laser Interferometer Gravitational-wave Observatory. *Reports on Progress in Physics*, 72(7):076901+, July 2009. URL: <http://dx.doi.org/10.1088/0034-4885/72/7/076901>, doi:10.1088/0034-4885/72/7/076901.
- [23] Rana Adhikari. *Sensitivity and noise analysis of 4 km laser interferometric gravitational wave antennae*. PhD thesis, Massachusetts Institute of Technology, July 2006. URL: <http://dspace.mit.edu/handle/1721.1/28646>.
- [24] Stefan Ballmer. *LIGO interferometer operating at design sensitivity with application to gravitational radiometry*. PhD thesis, Massachusetts Institute of Technology, June 2006. URL: <http://dspace.mit.edu/handle/1721.1/36396>.
- [25] Malik Rakhmanov. *Dynamics of Laser Interferometric Gravitational Wave Detectors*. PhD thesis, California Institute of Technology, May 2000. URL: <http://www.ligo.caltech.edu/docs/P/P000002-00.pdf>.

- [26] Peter Fritschel, Rolf Bork, Gabriela González, Nergis Mavalvala, Dale Ouimette, Haisheng Rong, Daniel Sigg, and Michael Zucker. Readout and Control of a Power-Recycled Interferometric Gravitational-Wave Antenna. *Appl. Opt.*, 40(28):4988–4998, October 2001. URL: <http://www.ligo.caltech.edu/docs/P/P000008-A.pdf>, doi: 10.1364/AO.40.004988.
- [27] R. W. P. Drever, J. L. Hall, F. V. Kowalski, J. Hough, G. M. Ford, A. J. Munley, and H. Ward. Laser phase and frequency stabilization using an optical resonator. *Applied Physics B: Lasers and Optics*, 31(2):97–105, June 1983. URL: <http://dx.doi.org/10.1007/BF00702605>, doi:10.1007/BF00702605.
- [28] Eric D. Black. An introduction to Pound–Drever–Hall laser frequency stabilization. *American Journal of Physics*, 69(1):79–87, January 2001. URL: <http://dx.doi.org/10.1119/1.1286663>, doi:10.1119/1.1286663.
- [29] Daniel Sigg and others. Frequency response of the LIGO interferometer. Technical Report T970084-00, LIGO Laboratory, February 1997. URL: <http://www.ligo.caltech.edu/docs/T/T970084-00.pdf>.
- [30] T. M. Niebauer, R. Schilling, K. Danzmann, A. Rüdiger, and W. Winkler. Nonstationary shot noise and its effect on the sensitivity of interferometers. *Physical Review A*, 43(9):5022–5029, May 1991. URL: <http://dx.doi.org/10.1103/PhysRevA.43.5022>, doi:10.1103/PhysRevA.43.5022.
- [31] Torrey T. Lyons, Martin W. Regehr, and Frederick J. Raab. Shot Noise in Gravitational-Wave Detectors with Fabry-Perot Arms. *Appl. Opt.*, 39(36):6761–6770, December 2000. URL: <http://dx.doi.org/10.1364/AO.39.006761>, doi:10.1364/AO.39.006761.
- [32] N. Mio. Observation of an effect due to non-stationary shot noise. *Physics Letters A*, 164(3-4):255–258, April 1992. URL: [http://dx.doi.org/10.1016/0375-9601\(92\)91100-6](http://dx.doi.org/10.1016/0375-9601(92)91100-6), doi:10.1016/0375-9601(92)91100-6.
- [33] Brian J. Meers and Kenneth A. Strain. Modulation, signal, and quantum noise in interferometers. *Physical Review A*, 44(7):4693–4703, October 1991. URL: <http://dx.doi.org/10.1103/PhysRevA.44.4693>, doi:10.1103/PhysRevA.44.4693.
- [34] Alessandra Buonanno, Yanbei Chen, and Nergis Mavalvala. Quantum noise in laser-interferometer gravitational-wave detectors with a heterodyne readout scheme. *Physical Review D*, 67(12):122005+, June 2003. URL: <http://dx.doi.org/10.1103/PhysRevD.67.122005>, doi:10.1103/PhysRevD.67.122005.
- [35] M. Evans, N. Mavalvala, P. Fritschel, R. Bork, B. Bhawal, R. Gustafson, W. Kells, M. Landry, D. Sigg, R. Weiss, S. Whitcomb, and H. Yamamoto. Lock acquisition of a gravitational-wave interferometer. *Opt. Lett.*, 27(8):598–600, April 2002. URL: <http://authors.library.caltech.edu/5527/1/EVAo102.pdf>, doi:10.1364/OL.27.000598.

- [36] Philip C. D. Hobbs. *Building Electro-Optical Systems: Making It all Work (Wiley Series in Pure and Applied Optics)*. Wiley, 2 edition, August 2009. URL: <http://www.amazon.com/exec/obidos/redirect?tag=citeulike07-20&path=ASIN/0470402296>.
- [37] Carlton M. Caves. Quantum-Mechanical Radiation-Pressure Fluctuations in an Interferometer. *Physical Review Letters*, 45(2):75–79, July 1980. URL: <http://dx.doi.org/10.1103/PhysRevLett.45.75>, doi:10.1103/PhysRevLett.45.75.
- [38] W. Chaibi and F. Bondu. Optomechanical issues in the gravitational wave detector advanced VIRGO. *Comptes rendus de l'Académie des Sciences*, in press.
- [39] Thomas R. Corbitt. *Quantum Noise and Radiation Pressure Effects in High Power Optical Interferometers*. PhD thesis, Massachusetts Institute of Technology, August 2008. URL: <http://hdl.handle.net/1721.1/45452>.
- [40] Matthew Evans. Optickle. Technical Report T070260-00, LIGO Laboratory, October 2007. URL: <http://www.ligo.caltech.edu/docs/T/T070260-00.pdf>.
- [41] H. Kogelnik and T. Li. Laser Beams and Resonators. *Appl. Opt.*, 5(10):1550–1567, October 1966. URL: <http://dx.doi.org/10.1364/AO.5.001550>, doi:10.1364/AO.5.001550.
- [42] A. E. Siegman. *Lasers*. University Science Books, October 1990. URL: <http://www.amazon.com/exec/obidos/redirect?tag=citeulike07-20&path=ASIN/0935702113>.
- [43] Volker Quetschke, Qi-Ze Shu, Guido Mueller, David Reitze, and David Tanner. Complex Modulation. Technical Report T070197-00-R, LIGO Scientific Collaboration, University of Florida, August 2007. URL: <https://dcc.ligo.org/cgi-bin/private/DocDB/ShowDocument?docid=27868>.

Vita

Tobin Fricke was born in Los Angeles, California in 1980. He studied Electrical Engineering and Computer Science (EECS) and Mathematics at the University of California, Berkeley.